Noname manuscript No.
(will be inserted by the editor)

Semi-implicit hybrid finite volume/finite element method for the GPR model of continuum mechanics

Saray Busto* · **Laura Río-Martín**

Received: date / Accepted: date

Abstract We present a new hybrid semi-implicit finite volume / finite element numerical scheme for the solution of incompressible and weakly compressible media. From the continuum mechanics model proposed by Godunov, Peshkov and Romenski (GPR), we derive the incompressible GPR formulation as well as a weakly compressible GPR system. As for the original GPR model, the new formulations are able to describe different media, from elastoplastic solids to viscous fluids, depending on the values set for the model's relaxation parameters. Then, we propose a new numerical method for the solution of both models based on the splitting of the original systems into three subsystems: one containing the convective part and non-conservative products, a second subsystem for the source terms of the distortion tensor and thermal impulse equations and, finally, a pressure subsystem. In the first stage of the algorithm, the transport subsystem is solved by employing an explicit finite volume method, while the source terms are solved implicitly. Next, the pressure subsystem is implicitly discretised using continuous finite elements. This methodology employs unstructured grids, with the pressure defined in the primal grid and the rest of the variables computed in the dual grid. To evaluate the performance of the proposed scheme, a numerical convergence analysis is carried out, which confirms the second order of accuracy in space. A wide range of benchmarks is reproduced for the incompressible and weakly compressible cases, considering both solid and fluid media. These results demonstrate the good behaviour and robustness of the proposed scheme in a variety of scenarios and conditions.

Keywords Semi-implicit structure-preserving scheme; finite volume methods; finite element methods; continuum mechanics; GPR model.

S. Busto (* corresponding author)
Department of Applied Mathematics, Universidade de Santiago de Compostela, 15782 Santiago de Compostela, Spain; Galician Center for Mathematical Research and Technology, CITMAga, 15782 Santiago de Compostela, Spain E-mail: saray.busto.ulloa@usc.es
Laura Río-Martín
Department of Information Engineering and Computer Science, University of Trento, Via Sommarive 9, Povo, 38123 Trento, Italy; Laboratory of Applied Mathematics, DICAM, University of Trento, Via Mesiano 77, 38123 Trento, Italy E-mail: laura.delrio@unitn.it

1 Introduction

Incompressible and weakly compressible flows appear in numerous industrial and biological applications, ranging from fluid dynamics in hydraulic systems to the study of airflow in aeronautical engineering. The study of such flows is crucial because of their prevalence in situations where the flow velocity is low compared to the speed of sound, making compressibility effects small but generally not negligible. To accurately model these flows, a classical approach is the use of Navier-Stokes equations, whose numerical solution has been extensively studied. A recently developed alternative is the use of the Godunov-Peshkov-Romenski (GPR) model for continuum mechanics, which offers a unified formulation for modelling different media, from solids with large deformations to compressible viscous fluids. The use of this model allows for capturing complex phenomena of continuum mechanics, providing greater versatility in the simulations than former classical approaches.

The main objective of this work is to present a novel methodology for addressing problems in the weakly compressible regime by solving incompressible and weakly compressible formulations of the GPR first-order hyperbolic model of continuum mechanics [39,66,74]. The compressible GPR model, which employs a single system of hyperbolic equations, describes both solids and fluids in a unified manner by an appropriate choice of the model relaxation parameters. This model originates from the elastoplastic deformation model of Godunov and Romenski [49], and was first introduced in [66]. Meanwhile, the heat equation is derived from the model proposed by Malyshev and Romenski in [57] and implemented in [73,72].

Since its introduction, the compressible GPR model has been successfully applied to model a variety of problems, including non-Newtonian and viscous flows, and elastic, elastoplastic and porous solids [39,15,65,41,53,64,70,71]. In addition, it has been extended to include the effects of electrodynamics [40], surface tension [31] or general relativity [69], as well as to model nonlinear dispersive systems [35] and to include solids or viscous fluids in multiphase systems [44]. Different types of schemes have been successfully developed to solve these equations as explicit finite volume (FV) methods [36], semi-implicit second order finite volume schemes [14,65], high order IMEX methods [52,10], high order ADER-FV and ADER-DG approaches [39,15,40,18], or smooth particle methods (SPH) [54].

It is noteworthy to remark that the GPR model presents a wide set of properties at the continuous level that should be conveyed to the discrete level. Firstly, the model falls within the framework of Symmetric Hyperbolic Thermodynamically Compatible (SHTC) systems so that thermodynamically compatibility at the discrete level may also be pursued, as done in the modern family of HTC-FV and HTC-DG schemes [22,19,2,21]. Moreover, the model presents natural involution constraints on the curl-free property of the distortion and thermal impulse fields that have been addressed, e.g., in [14]. We furthermore highlight the asymptotic preserving property of the model in the fluid relaxation limit, i.e., as the corresponding relaxation times go to zero, the Navier-Stokes-Fourier limit is obtained, [39]. To the best of the authors knowledge, simultaneous preservation of all these properties at the discrete level has not been achieved yet, and the effort is first placed on developing efficient schemes preserving at least some of these properties. In particular, the methodology proposed in this paper falls in the family of asymp-

totic preserving schemes in the fluid limit of the model. Furthermore, analogously to the asymptotic preserving properties of the Navier-Stokes equations in the incompressible limit, considering the low Mach limit, we recover an incompressible formulation of the GPR model.

Let us note that addressing low Mach number flows using the Navier-Stokes equations is a wide field of research where two main approaches have been initially followed: the development of explicit density-based and pressure-based solvers. The first family was first proposed in the framework of high Mach number flows and has as its main shortcoming the highly restrictive time step condition related to the pressure wave velocity in the low Mach number limit. Moreover, unless properly corrected, those schemes may present excessive numerical diffusivity due to an incorrect scaling with respect to the Mach number, [51,33,55]. On the other hand, the second family has been initially designed in the context of incompressible flows and is usually based on a non-conservative formulation of the equations, leading to important errors in the presence of strong discontinuities, [30,58]. Aiming at profiting from the main advantages of both families, the first semi-implicit pressure-based solvers were proposed in [61,85]. Since then, they have been successfully extended to different families of numerical methods including, e.g., finite volume approaches (FV), [32,38,7,12,80,16], discontinuous Galerkin schemes (DG), [79, 28,17,76], or hybrid finite volume/finite element methods (hybrid FV/FE), [6,25, 4,26] and hybrid finite volume/virtual element schemes (hybrid FV/VEM), [11, 8].

The same advantages and drawbacks arising in the discretisation of low Mach number flows when using the Navier-Stokes equations could also be expected for discretising the weakly compressible GPR model. Therefore, accounting for the promising results obtained in the framework of the Navier-Stokes equations and also in previous semi-implicit schemes for continuum mechanics models, [1,14], we focus on the development of a semi-implicit scheme for the incompressible and weakly compressible GPR models. In particular, the methodology presented in this paper follows the seminal ideas in [6] and is based on a semi-implicit hybrid scheme that combines finite volume and finite element methods, taking advantage of the benefits of both numerical approaches. This family of semi-implicit hybrid FV/FE schemes has been developed in the last decade aiming at solving the Navier-Stokes equations, both for incompressible and all Mach number flows as well as the shallow water and the MHD equations, on fixed and moving staggered unstructured grids in two and three spatial dimensions [25,26,67,20,24,43, 87,56]. The procedure behind this methodology consists of splitting the system into two parts, which decouples the pressure field from the convective system. This division of the original system into subsystems is performed following the Toro-Vázquez splitting technique [83]. Then, a second-order explicit finite volume discretisation is used for the convective terms, while a second-order continuous Lagrangian finite element scheme is employed to solve the pressure subsystem. Moreover, within this methodology, unstructured staggered grids are considered, similar to that described in [78,79,28]. Since we focus on the weakly compressible regime, the semi-implicit approach further improves the stability properties and the efficiency of the scheme with respect to classical fully explicit approaches.

This paper is organised as follows. Section 2 presents a brief review of the original GPR model, followed by the novel derivation of the related incompressible and weakly compressible GPR formulations. Section 3 details the proposed

numerical discretisation for both systems. In particular, the splitting performed to get the transport and the Poisson-type pressure subsystem is described. Then, the algorithms used to solve both subsystems are detailed, as well as the interpolation approach performed between the dual and the primal grids. Numerical validation of the proposed methodology is presented in Section 4 for two and three dimensions. The wide set of benchmarks studied includes both incompressible and weakly compressible cases, considering both solid and fluid media. The paper closes with some remarks and an outlook for future work in Section 5.

2 Governing equations

Before introducing the incompressible and the weakly compressible GPR models, we start recalling the original compressible Godunov-Peshkov-Romenski model for continuum mechanics [39,66,41], which reads

$$\frac{\partial}{\partial t}\rho + \frac{\partial}{\partial x_k}\left(\rho u_k\right) = 0, \tag{1a}$$

$$\frac{\partial}{\partial t}\left(\rho u_i\right) + \frac{\partial}{\partial x_k}\left(\rho u_i u_k\right) + \frac{\partial}{\partial x_i}p + \frac{\partial}{\partial x_k}\left(\sigma_{ik} + \omega_{ik}\right) = \rho g_i, \tag{1b}$$

$$\frac{\partial}{\partial t}A_{ik} + \frac{\partial}{\partial x_k}\left(u_m A_{im}\right) + u_j\left(\frac{\partial}{\partial x_j}A_{ik} - \frac{\partial}{\partial x_k}A_{ij}\right) = -\frac{1}{\theta_1\left(\tau_1\right)}E_{A_{ik}}, \tag{1c}$$

$$\frac{\partial}{\partial t}J_k + \frac{\partial}{\partial x_k}\left(J_m u_m\right) + \frac{\partial}{\partial x_k}T + u_j\left(\frac{\partial}{\partial x_j}J_k - \frac{\partial}{\partial x_k}J_j\right) = -\frac{1}{\theta_2\left(\tau_2\right)}E_{J_k}, \tag{1d}$$

$$\frac{\partial}{\partial t}\left(\rho S\right) + \frac{\partial}{\partial x_k}\left(\rho S u_k\right) + \frac{\partial}{\partial x_k}\left(\rho E_{J_k}\right) = \frac{\rho}{T}\left(\frac{1}{\theta_1\left(\tau_1\right)}E_{A_{ik}}E_{A_{ik}} + \frac{1}{\theta_2\left(\tau_2\right)}E_{J_k}E_{J_k}\right) \geq 0, \tag{1e}$$

$$\frac{\partial}{\partial t}\left(\rho E\right) + \frac{\partial}{\partial x_k}\left(\rho E u_k\right) + \frac{\partial}{\partial x_k}\left(p u_k\right) + \frac{\partial}{\partial x_k}\left(u_i \sigma_{ik}\right) + \frac{\partial}{\partial x_k}\left(u_i \omega_{ik}\right) + \frac{\partial}{\partial x_k}q_k = \rho g_i u_i. \tag{1f}$$

In this paper, we apply the Einstein summation notation for repeated indexes. Moreover, we denote ρ the density, $\mathbf{u} = (u_1, u_2, u_3)$ the velocity vector and its components, p the pressure, $\mathbf{A} = (A_{ik})$ the distortion field, given by a 3×3 tensor, $\mathbf{J} = (J_1, J_2, J_3)$ the thermal impulse vector, S the entropy, E the total energy, to be further described later, and $\mathbf{g} = (g_1, g_2, g_3)$ the gravity vector. The non-isotropic part of the stress tensor, containing the shear and thermal stresses, is given by:

$$\sigma_{ik} = A_{ji}\,\partial_{A_{jk}}(\rho E) = \rho c_s^2 G_{ij}\mathring{G}_{jk}, \qquad \omega_{ik} = J_i\,\partial_{J_k}(\rho E) = \rho c_h^2 J_i J_k, \tag{2}$$

where c_s^2 and c_h^2 are the characteristic velocities for the propagation of shear and thermal perturbations while $\mathring{G}_{ik}$ denotes the trace-free part of the metric tensor $G_{ik} = A_{ji}A_{jk}$,

$$\mathring{G}_{ik} = G_{ik} - \frac{1}{3}G_{mm}\delta_{ik}.$$

The heat flux is

$$q_k = \partial_{\rho S}\left(\rho E\right)\partial_{J_k}\left(\rho E\right) = \rho c_h^2 T J_k, \tag{3}$$

and T corresponds to the temperature

$$T = \partial_{\rho S}\left(\rho E\right).$$

Furthermore, the shear and thermal stress relaxation functions read

$$\theta_1\left(\tau_1\right) = \frac{1}{3}\rho_0\tau_1 c_s^2\left|\mathbf{A}\right|^{-\frac{5}{3}}, \qquad \theta_2\left(\tau_2\right) = \frac{\rho_0 T_0}{T}\tau_2 c_h^2, \tag{4}$$

with τ_1 and τ_2 the corresponding relaxation times. The total energy E can be divided into four terms as

$$E\left(\rho,\mathbf{u},\mathbf{A},\mathbf{J},S\right) = E_1\left(\mathbf{u}\right) + E_2\left(\mathbf{A}\right) + E_3\left(\mathbf{J}\right) + E_4\left(\rho,S\right), \tag{5}$$

while in case the thermal impulse contributions are neglected, the term E_3 is no longer considered. The first contribution to the energy, E_1, corresponds to the specific kinetic energy per unit mass,

$$E_1\left(\mathbf{u}\right) = \frac{1}{2}\left|\mathbf{u}\right|^2. \tag{6}$$

The second and third terms provide the contribution of the mesoscopic, non-equilibrium, part of the total energy related to the material deformations and the thermal impulse,

$$E_2\left(\mathbf{A}\right) = \frac{1}{4}c_s^2\mathring{G}_{ij}\mathring{G}_{ij}, \qquad E_3\left(\mathbf{J}\right) = \frac{1}{2}c_h^2 J_i J_i. \tag{7}$$

The last term in (5) is the internal energy, related to the kinetic energy of the molecular motion, that we assume given by the ideal gas equation of state

$$E_4\left(\rho,S\right) = \frac{\rho^{\gamma-1}}{\left(\gamma-1\right)}e^{\frac{S}{c_v}},$$

which is equivalent to consider

$$E_4\left(\rho,p\right) = \frac{p}{\rho\left(\gamma-1\right)}, \tag{8}$$

with $\gamma = \frac{c_p}{c_v}$ the specific heat ratio at constant pressure, c_p, and at constant volume, c_v.

2.1 Incompressible GPR model

To get the simplified GPR model in the incompressible limit, we proceed as for the incompressible Navier-Stokes equations. Accordingly, we suppose the fluid to be incompressible, homogeneous and non heat-conducting, obtaining the following system of conservation laws:

$$\frac{\partial}{\partial x_k}\left(\rho u_k\right) = 0, \tag{9a}$$

$$\frac{\partial}{\partial t}\left(\rho u_i\right) + \frac{\partial}{\partial x_k}\left(\rho u_i u_k\right) + \frac{\partial}{\partial x_i}p + \frac{\partial}{\partial x_k}\sigma_{ik} = \rho g_i, \tag{9b}$$

$$\frac{\partial}{\partial t}A_{ik} + \frac{\partial}{\partial x_k}\left(u_m A_{im}\right) + u_j\left(\frac{\partial}{\partial x_j}A_{ik} - \frac{\partial}{\partial x_k}A_{ij}\right) = -\frac{1}{\theta_1\left(\tau_1\right)}E_{A_{ik}}, \tag{9c}$$

where we have furthermore assumed a constant density.

2.2 Weakly compressible GPR model

On the other hand, a pressure-based reformulation of the entropy equation provides a PDE system able to solve a weakly compressible medium. Since the pressure can be written as a function of the density and entropy,

$$p = \rho^{\gamma} e^{\frac{S}{c_v}},$$

$\gamma = \dfrac{c^2\rho}{p}$ and denoting $\dfrac{d}{dt}$ the material derivative, we have

$$\frac{\partial p}{\partial t} + u\cdot\nabla p = \frac{dp}{dt} = \frac{\partial p}{\partial \rho}\frac{d\rho}{dt} + \frac{\partial p}{\partial S}\frac{dS}{dt} = -\rho c^2 \mathrm{div}\mathbf{u} + \rho T\left(\gamma-1\right)\frac{dS}{dt}. \tag{10}$$

On the other hand, from (1e) and (1a), we get

$$\frac{dS}{dt} = \frac{\partial}{\partial t}S + u_k\frac{\partial}{\partial x_k}S = -\frac{1}{\rho}\frac{\partial}{\partial x_k}\left(\rho E_{J_k}\right) + \frac{1}{T}\left(\frac{1}{\theta_1\left(\tau_1\right)}E_{A_{ik}}E_{A_{ik}} + \frac{1}{\theta_2\left(\tau_2\right)}E_{J_k}E_{J_k}\right).$$

Substitution in (10) yields

$$\begin{aligned}\frac{\partial p}{\partial t} + u_k\frac{\partial}{\partial x_k}p + c^2\frac{\partial}{\partial x_k}\left(\rho u_k\right) - c^2 u_k\frac{\partial}{\partial x_k}\rho + c_h^2\left(\gamma-1\right)T\frac{\partial}{\partial x_k}\left(\rho J_k\right)\\ = \left(\gamma-1\right)\left(\frac{\rho}{\theta_1\left(\tau_1\right)}E_{A_{ik}}E_{A_{ik}} + \frac{\rho}{\theta_2\left(\tau_2\right)}E_{J_k}E_{J_k}\right).\end{aligned}$$

Or, equivalently,

$$\begin{aligned}\frac{\partial p}{\partial t} + \mathbf{u}\cdot\nabla p + c^2\,\nabla\cdot\left(\rho\mathbf{u}\right) - c^2\mathbf{u}\cdot\nabla\rho + c_h^2\left(\gamma-1\right)T\,\nabla\cdot\left(\rho\mathbf{J}\right)\\ = \left(\gamma-1\right)\left(\frac{\rho}{\theta_1\left(\tau_1\right)}\mathbf{E_A}\cdot\mathbf{E_A} + \frac{\rho}{\theta_2\left(\tau_2\right)}\mathbf{E_J}\cdot\mathbf{E_J}\right).\end{aligned}$$

Therefore, the weakly compressible GPR model, where the entropy equation has been replaced by a non-conservative pressure equation, reads:

$$\frac{\partial}{\partial t}\rho + \frac{\partial}{\partial x_k}\left(\rho u_k\right) = 0, \tag{11a}$$

$$\frac{\partial}{\partial t}\left(\rho u_i\right) + \frac{\partial}{\partial x_k}\left(\rho u_i u_k\right) + \frac{\partial}{\partial x_i}p + \frac{\partial}{\partial x_k}\left(\sigma_{ik}+\omega_{ik}\right) = \rho g_i, \tag{11b}$$

$$\frac{\partial}{\partial t}A_{ik} + \frac{\partial}{\partial x_k}\left(u_m A_{im}\right) + u_j\frac{\partial}{\partial x_j}A_{ik} - u_j\frac{\partial}{\partial x_k}A_{ij} = -\frac{1}{\theta_1\left(\tau_1\right)}E_{A_{ik}}, \tag{11c}$$

$$\frac{\partial}{\partial t}J_k + \frac{\partial}{\partial x_k}\left(J_m u_m\right) + \frac{\partial}{\partial x_k}T + u_j\left(\frac{\partial}{\partial x_j}J_k - \frac{\partial}{\partial x_k}J_j\right) = -\frac{1}{\theta_2\left(\tau_2\right)}E_{J_k}, \tag{11d}$$

$$\begin{aligned}\frac{\partial p}{\partial t} + u_k\frac{\partial}{\partial x_k}p + c^2\frac{\partial}{\partial x_k}\left(\rho u_k\right) - c^2 u_k\frac{\partial}{\partial x_k}\rho + c_h^2\left(\gamma-1\right)T\frac{\partial}{\partial x_k}\left(\rho J_k\right)\\ = \frac{\left(\gamma-1\right)\rho}{\theta_1\left(\tau_1\right)}E_{A_{ik}}E_{A_{ik}} + \frac{\left(\gamma-1\right)\rho}{\theta_2\left(\tau_2\right)}E_{J_k}E_{J_k}.\end{aligned} \tag{11e}$$

Let us remark that, due to thermodynamical compatibility, the non-conservative pressure equation could also be obtained using the total energy conservation equation instead of the entropy equation, as shown in Appendix A.

3 Numerical discretisation

The discretisation of the former GPR systems will be performed in the framework of the hybrid finite volume/finite element approach introduced in [6,25,4,26,67, 23] for incompressible, weakly compressible, and all Mach number flows and the shallow water equations. In particular, we are interested in the low Mach number limit, so we first address the incompressible GPR model (9), and we then also propose a hybrid FV/FE approach for the discretisation of a pressure-based formulation of (11) able to address weakly compressible flows.

3.1 Semi-discretisation in time of the incompressible GPR model

A semi-discretisation in time of the system (9) yields

$$\frac{\partial}{\partial x_k}\left(\rho u_k^{n+1}\right) = 0, \tag{12a}$$

$$\frac{1}{\Delta t}\left(\rho u_i^{n+1} - \rho u_i^{n}\right) + \frac{\partial}{\partial x_k}\left(\rho u_i^n u_k^n\right) + \frac{\partial}{\partial x_i} p^{n+1} + \frac{\partial}{\partial x_k}\sigma_{ik}^n = \rho^n g_i, \tag{12b}$$

$$\frac{1}{\Delta t}\left(A_{ik}^{n+1} - A_{ik}^{n}\right) + \frac{\partial}{\partial x_k}\left(u_m^n A_{im}^n\right) + u_j^n \frac{\partial}{\partial x_j} A_{ik}^n - u_j^n \frac{\partial}{\partial x_k} A_{ij}^n = -\frac{1}{\theta_1^{n+1}(\tau_1)} E_{A_{ik}}^{n+1}. \tag{12c}$$

Following classical projection methods, [62,50,25], we split the momentum equation into two parts and gather the equations into a transport and a pressure subsystem:

Transport subsystem

$$\rho u_i^* = \rho u_i^n - \Delta t\left(\frac{\partial}{\partial x_k}\left(\rho u_i^n u_k^n\right) + \frac{\partial}{\partial x_i} p^n + \frac{\partial}{\partial x_k}\sigma_{ik}^n - \rho^n g_i\right), \tag{13a}$$

$$A_{ik}^{n+1} = A_{ik}^n - \Delta t\left(\frac{\partial}{\partial x_k}\left(u_m^n A_{im}^n\right) + u_j^n \frac{\partial}{\partial x_j} A_{ik}^n - u_j^n \frac{\partial}{\partial x_k} A_{ij}^n + \frac{1}{\theta_1^{n+1}(\tau_1)} E_{A_{ik}}^{n+1}\right). \tag{13b}$$

Pressure subsystem

$$\frac{\partial}{\partial x_k}\left(\rho u_k^{n+1}\right) = 0, \tag{14a}$$

$$\rho u_i^{n+1} = \rho u_i^* - \Delta t \frac{\partial}{\partial x_i}\delta p^{n+1}, \qquad \delta p^{n+1} = p^{n+1} - p^n. \tag{14b}$$

Taking into account the nature of these systems, we will employ an explicit finite volume approach for the spatial discretisation of (13) while (14a)-(14b) will be solved implicitly using continuous finite elements.

3.2 Semi-discretisation in time of the weakly compressible GPR model

Similarly, for the weakly compressible GPR model (11), we apply a splitting procedure following [83] and, introducing the semi-discretisation in time, we get

$$\frac{1}{\Delta t}\left(\rho^{n+1}-\rho^{n}\right)+\frac{\partial}{\partial x_k}\left(\rho u_k^{n+1}\right)=0, \tag{15a}$$

$$\frac{1}{\Delta t}\left(\rho u_i^{*}-\rho u_i^{n}\right)+\frac{\partial}{\partial x_k}\left(\rho u_i^{n}u_k^{n}\right)+\frac{\partial}{\partial x_k}\sigma_{ik}^{n}+\frac{\partial}{\partial x_k}\omega_{ik}^{n}=\rho^{n}g_i, \tag{15b}$$

$$\frac{1}{\Delta t}\left(\rho u_i^{n+1}-\rho u_i^{*}\right)+\frac{\partial}{\partial x_i}p^{n+1}=0, \tag{15c}$$

$$\frac{1}{\Delta t}\left(A_{ik}^{n+1}-A_{ik}^{n}\right)+\frac{\partial}{\partial x_k}\left(u_m^{n}A_{im}^{n}\right)+u_j^{n}\frac{\partial}{\partial x_j}A_{ik}^{n}-u_j^{n}\frac{\partial}{\partial x_k}A_{ij}^{n}=-\frac{1}{\theta_1^{n+1}\left(\tau_1\right)}E_{A_{ik}}^{n+1}, \tag{15d}$$

$$\frac{1}{\Delta t}\left(J_k^{n+1}-J_k^{n}\right)+\frac{\partial}{\partial x_k}(J_m^{n}u_m^{n})+\frac{\partial}{\partial x_k}T^{n}+u_j^{n}\left(\frac{\partial}{\partial x_j}J_k^{n}-\frac{\partial}{\partial x_k}J_j^{n}\right)=-\frac{1}{\theta_2^{\star}\left(\tau_2\right)}E_{J_k}^{n+1}, \tag{15e}$$

$$\frac{1}{\Delta t}\left(\widetilde{p}_p-p^{n}\right)+u_k^{n}\frac{\partial}{\partial x_k}p^{n}+c_h^{2}\left(\gamma-1\right)T^{n}\frac{\partial}{\partial x_k}\left(\rho^{n}J_k^{n}\right)=\mathcal{S}^{p}\left(\mathbf{Q}^{n+1}\right), \tag{15f}$$

$$\frac{1}{\Delta t}\widetilde{p}_\rho-c^{2}u_k^{n}\frac{\partial}{\partial x_k}\rho^{n}=0, \tag{15g}$$

$$\frac{1}{\Delta t}\left(p^{n+1}-\widetilde{p}\right)+c^{2}\frac{\partial}{\partial x_k}\left(\rho u_k^{n+1}\right)=0. \tag{15h}$$

with

$$\mathcal{S}^{p}\left(\mathbf{Q}^{n+1}\right)=\frac{\rho^{n+1}\left(\gamma-1\right)}{\theta_1^{n+1}\left(\tau_1\right)}E_{A_{ik}}^{n+1}E_{A_{ik}}^{n+1}+\frac{\rho^{n+1}\left(\gamma-1\right)}{\theta_2^{\star}\left(\tau_2\right)}E_{J_k}^{n+1}E_{J_k}^{n+1}$$

and $\mathbf{Q}=(\rho,\mathbf{u},\mathbf{A},\mathbf{J},p)$. As for the incompressible GPR model, gathering (15c) and (15h), we get a pressure system of the form

$$\frac{1}{\Delta t}\left(p^{n+1}-\widetilde{p}\right)+c^{2}\frac{\partial}{\partial x_k}\left(\rho u_k^{n+1}\right)=0, \tag{16a}$$

$$\rho u_i^{n+1}=\rho u_i^{*}-\Delta t\frac{\partial}{\partial x_i}p^{n+1}, \tag{16b}$$

corresponding to a Poisson-type problem and a set of transport equations containing the conservative fluxes and non-conservative products, (15a)-(15b), (15d)-(15g).

3.2.1 Asymptotic preserving property in the incompressible limit

The GPR model is endowed with two types of asymptotic limits. On the one hand, the fluid and solid limits of the model can be retrieved adequately setting the relaxation times τ_1 and τ_2, a behaviour that is inherited by the weakly compressible and the incompressible GPR models. On the other hand, for a homogeneous non-heat-conducting incompressible medium, we get the incompressible GPR model. This limit corresponds to the low Mach number limit of the compressible Navier-Stokes equations when considering the fluid limit of the GPR model. Further, the

GPR model extends this concept to the solid mechanics framework. Therefore, it is important to construct numerical schemes compatible with this AP property also at the discrete level. The proposed splitting approach in time verifies the AP property in the incompressible limit by construction. Taking the incompressible limit yields to $c^2 \to \infty$ so only the terms of order c^2 are retained in the limit case for equations (15f)-(15h). Next, assuming the medium to be homogeneous, leads to

$$\frac{\partial}{\partial x_k}\left(\rho u_k^{n+1}\right) = 0$$

which, together with (15c) form the elliptic pressure problem obtained for the incompressible model formulated in terms of p^{n+1}. As expected, this system coincides with the classical pressure subsystem for pressure-based discretizations of the Navier-Stokes equations, [25,27]. Finally, since we assume the medium to be homogeneous and non-heat-conducting, equations (15a) and (15e) and the terms depending on ω_{ik} can be neglected yielding also to the transport system of the incompressible GPR model. Nonetheless, the spatial discretization employed for the incompressible GPR model does not exactly verify the divergence free condition for the velocity field. This shortcoming is inherited by the weakly GPR model which, in the incompressible limit, does not provide a divergence free solution up to machine precision but it yields errors that decrease at the order of the numerical method.

3.3 Overall algorithm

Attending to the nature of the different equations involved in (13)-(14) and (15), the proposed hybrid FV/FE methodology is divided into the following stages:

- Transport stage. The equations containing the convective and non-conservative terms, i.e., system (13) for the incompressible GPR model and equations (15a), (15b), (15d), (15e), and (15f) for the weakly compressible GPR model, are discretised explicitly using a finite volume scheme. Let us note that both systems can be recast in the general form

$$\partial_t \mathbf{Q} + \nabla \cdot \boldsymbol{\mathcal{F}}(\mathbf{Q}) + \boldsymbol{\mathcal{B}}(\mathbf{Q}) \cdot \nabla \mathbf{Q} = \boldsymbol{\mathcal{S}}(\mathbf{Q}), \tag{17}$$

  with $\mathbf{Q}$ the vector of conservative variables, $\boldsymbol{\mathcal{F}}(\mathbf{Q})$ the flux term, $\boldsymbol{\mathcal{B}}(\mathbf{Q}) \cdot \nabla \mathbf{Q}$ the non-conservative products, and $\boldsymbol{\mathcal{S}}(\mathbf{Q})$ the source terms.
- Interpolation stage. This stage is only necessary for the weakly GPR model where the contribution of the non-conservative product on the density derivative appearing in the pressure equation (15g), is approximated by making use of an explicit finite volume approach. Moreover, the pressure intermediate value $\widetilde{p}_p$ obtained in the dual cells during the convective stage is interpolated to the primal grid.
- Pressure stage. The pressure subsystems (14) or (16) are solved using continuous finite elements.
- Correction stage. In the case of incompressible flows, the use of the pressure gradient at the previous time step is not sufficient to ensure the divergence-free condition of the velocity field, so we must correct $\rho \mathbf{u}^*$ with the gradient of the pressure variation $\nabla \delta p^{n+1}$. On the other hand, for the weakly compressible

GPR model, the pressure gradient has been completely neglected in the convective stage, so we need to incorporate its contribution once the new pressure is available, ∇p^{n+1}. Therefore, the intermediate momentum $\rho \mathbf{u}^*$ is corrected using (14b) and (16b) for the incompressible and the weakly compressible GPR models, respectively.

In what follows, we introduce the spatial discretisation and provide a detailed description of each algorithm stage.

3.4 Spatial discretisation. Unstructured staggered grids

To discretise the computational domain we employ the so-called face-based or diamond-shaped staggered grids, [5,86,6,78]. We denote $\boldsymbol{\Upsilon} = \{T_{\boldsymbol{\kappa}},\, \boldsymbol{\kappa} = 1, \dots, M\}$ the tessellation corresponding to the primal grid composed of M triangular elements $T_{\boldsymbol{\kappa}}$. Then, each triangle $T_{\boldsymbol{\kappa}}$ is divided into three subtriangles having as base one of the boundary edges of $T_{\boldsymbol{\kappa}}$ and the opposite vertex the barycentre of $T_{\boldsymbol{\kappa}}$, denoted by $\mathbf{x}_{\boldsymbol{\kappa}}$. Merging the two subtriangles related to a boundary edge, we get an interior dual cell C_{i}. Meanwhile, for the element edges located at a boundary of the domain, the related dual element is simply taken to be the corresponding subtriangle inside the domain. A sketch of the dual mesh construction in 2D is depicted in Figure 1. For a detailed description of the unstructured faced-based staggered grids in 3D, we may refer to [4].

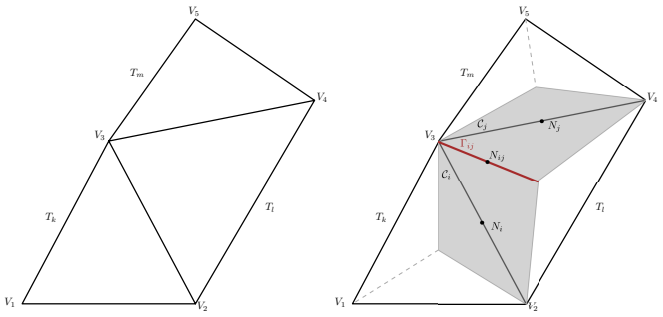

Fig. 1 Sketch of the face-based unstructured grids in 2D. Left: T_k, T_l, T_m are the triangles of the primal grid and V_j, $j = 1, \dots, 5$ are their vertices. Right: Interior (grey elements) and boundary (white elements) elements of the dual mesh. The boundary between the two interior dual cells C_{i} and C_{j}, Γ_{ij}, is highlighted in red.

The use of this kind of staggered grids is two-folded motivated. On the one hand, having a primal grid made of triangles/tetrahedra eases the tessellation of complex domains if compared with Cartesian grids made of quadrilaterals/hexahedra. On the other hand, the combination of two staggered grids, the primal one used within the pressure system discretisation and the dual one employed during the transport stage, avoids stability issues as the well-known checkerboard phenomenon that often appears when collocated grids are employed, [84]. Further, the use of this grid arrangement becomes useful for the design of a second order finite volume scheme with a very small stencil, as has already been shown in [25,4].

To complete the description of the spatial domain discretisation in 2D, we still need to introduce some notation to be employed in the description of the algorithm stages. Given a dual cell C_{i}, we denote $|C_{\mathrm{i}}|$ its area and $\Gamma_{\mathrm{i}} \equiv \partial C_{\mathrm{i}}$ its boundary. Taking into account the shape of the dual interior elements, Γ_{i} can be decomposed into four straight edges labelled as Γ_{ij}, with C_{i} and C_{j} the two dual cells sharing that edge. Similarly, for a boundary cell, we have three edges, two of them of the interior type Γ_{ij} and a boundary edge $\Gamma_{\mathrm{i}\Gamma}$. Moreover, $\mathbf{n}_{\mathrm{ij}}$ represents the unitary external normal of Γ_{ij}, and $\boldsymbol{\eta}_{\mathrm{ij}}$ the length-weighted normal, i.e., $\boldsymbol{\eta}_{\mathrm{ij}} = \mathbf{n}_{\mathrm{ij}}\,|\Gamma_{\mathrm{ij}}| = \mathbf{n}_{\mathrm{ij}}\,\|\boldsymbol{\eta}_{\mathrm{ij}}\|$ with $|\Gamma_{\mathrm{ij}}|$ the length of edge Γ_{ij}. Finally, $V_{\boldsymbol{\kappa}\mathfrak{l}}$, $\mathfrak{l} \in \{1,\dots,3\}$, refer to the three vertex of a primal element $T_{\boldsymbol{\kappa}}$ and $\mathbf{n}_{\boldsymbol{\kappa}}$ denotes its outward-pointing unit normal.

For the numerical results presented in Section 4, the primal simplex grids have been created using an external meshing software and then imported into the code using the mesh conversion tool FEconv, [63]. In case of 3D rectangular domains, regular unstructured meshes are generated within the code, using a standard methodology based on split Cartesian meshes, as detailed in [67].

3.5 Transport stage. Finite volume method in the dual grid

System (17) is discretised by employing an explicit finite volume method. Accordingly, we integrate (17) on each control volume C_{i} and apply the Gauss theorem to transform the integral of the flux term into the integral of the normal flux along the cell boundary, yielding to

$$\mathbf{Q}_{\mathrm{i}}^{*} = \mathbf{Q}_{\mathrm{i}}^{n} - \frac{\Delta t}{|C_{\mathrm{i}}|}\left(\int_{\Gamma_{\mathrm{i}}} \boldsymbol{\mathcal{F}}\left(\mathbf{Q}^{n}\right)\cdot\mathbf{n}_{\mathrm{i}}\,\mathrm{dS} + \int_{C_{\mathrm{i}}} \boldsymbol{\mathcal{B}}(\mathbf{Q}^{n})\cdot\nabla\,\mathbf{Q}^{n}\,\mathrm{dV} - \int_{C_{\mathrm{i}}} \boldsymbol{\mathcal{S}}\left(\mathbf{Q}\right)\mathrm{dV}\right), \quad (18)$$

with $\mathbf{Q}^{*} = \left(\rho^{n+1}, \rho\mathbf{u}^{*}, \mathbf{A}^{n+1}\right)^{T}$ for the incompressible GPR model and $\mathbf{Q}^{*} = \left(\rho^{n+1}, \rho\mathbf{u}^{*}, \mathbf{A}^{n+1}, \mathbf{J}^{n+1}, \widetilde{p}_{p}\right)^{T}$ for the weakly compressible GPR model. In what follows, to describe the FV scheme, we focus on the weakly compressible GPR case since the incompressible one can be seen just as a subcase of it.

3.5.1 Explicit treatment of the convective terms

The integral of the flux term is decomposed onto the sum of the contributions of the normal flux along each cell boundary as

$$\int_{\Gamma_{\mathrm{i}}} \boldsymbol{\mathcal{F}}\left(\mathbf{Q}^{n}\right)\cdot\mathbf{n}_{\mathrm{i}}\,\mathrm{dS} = \sum_{N_{\mathrm{j}}\in\mathcal{K}_{\mathrm{i}}} |\Gamma_{\mathrm{ij}}|\,\boldsymbol{\mathcal{F}}^{NF}\left(\overline{\mathbf{Q}}_{\mathrm{i}}^{n}, \overline{\mathbf{Q}}_{\mathrm{j}}^{n}, \mathbf{n}_{\mathrm{ij}}\right), \quad (19)$$

with $\mathcal{K}_{\mathrm{i}}$ the set of neighbours of C_{i} and $\boldsymbol{\mathcal{F}}^{NF}$ a numerical flux function. In particular, we employ the Rusanov numerical flux, [75],

$$\boldsymbol{\mathcal{F}}^{R}\left(\overline{\mathbf{Q}}_{\mathrm{i}}^{n}, \overline{\mathbf{Q}}_{\mathrm{j}}^{n}, \mathbf{n}_{\mathrm{ij}}\right) = \frac{1}{2}\left(\boldsymbol{\mathcal{F}}\left(\overline{\mathbf{Q}}_{\mathrm{i}}^{n}\right) + \boldsymbol{\mathcal{F}}\left(\overline{\mathbf{Q}}_{\mathrm{j}}^{n}\right)\right) - \alpha_{\mathrm{ij}}^{n}\left(\overline{\mathbf{Q}}_{j}^{n} - \overline{\mathbf{Q}}_{i}^{n}\right), \quad (20)$$

with the maximum signal speed on the edge

$$\alpha_{\mathrm{ij}}^{n} = \max\left\{\left|\overline{\mathbf{u}}_{\mathrm{i}}^{n}\cdot\mathbf{n}_{\mathrm{ij}} \pm c_{s}\right|, \left|\frac{3}{2}\overline{\mathbf{u}}_{\mathrm{i}}^{n}\cdot\mathbf{n}_{\mathrm{ij}} \pm c_{\mathrm{i}}\right|, \left|\overline{\mathbf{u}}_{\mathrm{j}}^{n}\cdot\mathbf{n}_{\mathrm{ij}} \pm c_{s}\right|, \left|\frac{3}{2}\overline{\mathbf{u}}_{\mathrm{j}}^{n}\cdot\mathbf{n}_{\mathrm{ij}} \pm c_{\mathrm{j}}\right|\right\},$$

$$c_{\mathrm{i}} = \sqrt{\frac{4}{3}c_s^2 + \frac{1}{4}\left|\mathbf{u}_{\mathrm{i}}\right|^2}, \tag{21}$$

for the incompressible GPR model and

$$\alpha_{\mathrm{ij}}^n = \max\left\{\left|\overline{\mathbf{u}}_{\mathrm{i}}^n \cdot \mathbf{n}_{\mathrm{ij}} \pm c_{\mathrm{i}}^n\right|, \left|\overline{\mathbf{u}}_{\mathrm{j}}^n \cdot \mathbf{n}_{\mathrm{ij}} \pm c_{\mathrm{j}}^n\right|\right\}, \qquad c_{\mathrm{i}}^n = \sqrt{\frac{4}{3}c_s^2 + \frac{2c_h^2\overline{T}_{\mathrm{i}}^n}{\left(\overline{\rho}_{\mathrm{i}}^n\right)^2 c_v}}, \tag{22}$$

for the weakly compressible GPR model. Besides, if we sought a first order scheme, $\overline{\mathbf{Q}}_{\mathrm{i}}$ and $\overline{\mathbf{Q}}_{\mathrm{j}}$ are simply taken as the values of $\mathbf{Q}$ at the two dual cells related to the dual edge, $\overline{\mathbf{Q}}_{\mathrm{i}} := \mathbf{Q}_{\mathrm{i}}$, $\overline{\mathbf{Q}}_{\mathrm{j}} := \mathbf{Q}_{\mathrm{j}}$. On the other hand, to attain second order, $\overline{\mathbf{Q}}_{\mathrm{i}}$ and $\overline{\mathbf{Q}}_{\mathrm{j}}$ must correspond to the half in time evolved boundary extrapolated values. More precisely, we consider the local ADER approach proposed in [25] and perform the following steps:

1. Piece-wise polynomial reconstruction. Given a variable Q, we build the left and right reconstruction polynomials related to edge Γ_{ij} as

$$P_{\mathrm{ij}}^L(\mathbf{x}) = Q_{\mathrm{i}} + (\mathbf{x} - \mathbf{x}_{\mathrm{i}})\,\nabla Q_{\mathrm{ij}}^L, \qquad P_{\mathrm{ij}}^R(\mathbf{x}) = Q_{\mathrm{j}} + (\mathbf{x} - \mathbf{x}_{\mathrm{j}})\,\nabla Q_{\mathrm{ij}}^R. \tag{23}$$

   The slopes ∇Q_{ij}^L and ∇Q_{ij}^R are computed using an ENO interpolation method so that the final scheme is nonlinear and, therefore, circumvents Godunov's theorem. Accordingly, denoting T_{ij} the primal element containing the face Γ_{ij} and T_{ij}^L and T_{ij}^R the two neighbour primal elements containing one halve of the dual cells C_{i} and C_{j}, the slopes are computed as

$$\nabla Q_{\mathrm{ij}}^L = \begin{cases} \nabla Q_{|T_{\mathrm{ij}}^L} \text{ if } \left|\nabla Q_{|T_{\mathrm{ij}}^L} \cdot (\mathbf{x}_{\mathrm{ij}} - \mathbf{x}_{\mathrm{i}})\right| \leq \left|\nabla Q_{|T_{\mathrm{ij}}} \cdot (\mathbf{x}_{\mathrm{ij}} - \mathbf{x}_{\mathrm{i}})\right|, \\ \nabla Q_{|T_{\mathrm{ij}}} \qquad \text{otherwise;} \end{cases} \tag{24}$$

$$\nabla Q_{\mathrm{ij}}^R = \begin{cases} \nabla Q_{|T_{\mathrm{ij}}^R} \text{ if } \left|\nabla Q_{|T_{\mathrm{ij}}^R} \cdot (\mathbf{x}_{\mathrm{ij}} - \mathbf{x}_{\mathrm{i}})\right| \leq \left|\nabla Q_{|T_{\mathrm{ij}}} \cdot (\mathbf{x}_{\mathrm{ij}} - \mathbf{x}_{\mathrm{i}})\right|, \\ \nabla Q_{|T_{\mathrm{ij}}} \qquad \text{otherwise.} \end{cases} \tag{25}$$

   The gradients $\nabla Q_{|T_{\mathrm{ij}}}$, $\nabla Q_{|T_{\mathrm{ij}}^L}$ and $\nabla Q_{|T_{\mathrm{ij}}^R}$ are computed in the primal cells using Crouzeix-Raviart finite elements which have as nodes the barycentres of the faces that are identified with the nodes of the dual cells.
2. Computation of boundary extrapolated data. The polynomials are evaluated in the barycentre of the dual edge, $\mathbf{x}_{\mathrm{ij}}$, obtaining the boundary extrapolated values Q_{i}^L and Q_{j}^R.
3. Half in time evolution. A midpoint rule, combined with the Cauchy-Kovalevskaya procedure to transform the time derivatives into spatial derivatives using the governing equations, provides the approximation of the conservative variables at time $t^n + \frac{1}{2}\Delta t$. Further details on this methodology and the original ADER approach can be found, e.g. in [26,81,82]. Moreover, for recent advances in ADER methods, including the ADER-DG approach which avoids the Cauchy-Kovalevskaya procedure by introducing a local space-time predictor, we refer to [37,18].

In the numerical results, Section 4, as an alternative to the ENO-based reconstruction introduced above, we also consider the use of the min-mod limiter of Roe, [68], and the Barth and Jespersen limiter, [3].

3.5.2 Pressure gradient in the incompressible GPR model

Let us note that the incompressible GPR model equation (12b) includes a term on the pressure gradient at the previous time step. Contrary to what is done in most Godunov-type methods, where this kind of term is included within the flux, [39,22], we compute it as if it was a source term since it does not depend on the pressure at the new time step and thus it does not need to be included in the convective terms nor in the CFL time step restriction of the explicit subsystem. Therefore, to approximate its contribution, we interpolate the pressure at the previous time step, which has been computed in the primal vertex, into the dual edges, p_{ij}^n, by simply taking the average between the two vertexes of each edge. In case one of the vertex corresponds to the barycentre of the primal element, its value is first obtained by averaging the pressure at the three vertex of the primal element. Finally, we compute

$$\int_{C_{\mathrm{i}}} \nabla p^n \,\mathrm{dV} = \sum_{N_{\mathrm{j}} \in \mathcal{K}_{\mathrm{i}}} p_{\mathrm{ij}}^n \boldsymbol{\eta}_{\mathrm{ij}}. \tag{26}$$

3.5.3 Path conservative discretisation of the non-conservative products

The non-conservative products, $\boldsymbol{\mathcal{B}}(\mathbf{Q}) \cdot \nabla \mathbf{Q}$, are discretised employing a path conservative scheme based on the straight line segment path, [59,29,46]. Accordingly, we approximate

$$\int_{C_{\mathrm{i}}} \boldsymbol{\mathcal{B}}(\mathbf{Q}^n) \cdot \nabla \mathbf{Q}^n \,\mathrm{dV} = \int_{\Gamma_{\mathrm{i}}} \mathcal{D}\left(\overline{\mathbf{Q}}^n\right) \cdot \mathbf{n}_{\mathrm{i}} \,\mathrm{dS} + \int_{C_{\mathrm{i}} \setminus \Gamma_{\mathrm{i}}} \boldsymbol{\mathcal{B}}(\overline{\mathbf{Q}}^n) \cdot \nabla \overline{\mathbf{Q}}^n \,\mathrm{dV}\,. \tag{27}$$

In Equation (27), the first term considers the jumps of the discrete solution across the cell boundaries for which we employ the boundary extrapolated values related to the face:

$$\int_{\Gamma_{\mathrm{i}}} \mathcal{D}\left(\overline{\mathbf{Q}}^n\right) \cdot \mathbf{n}_{\mathrm{i}} \,\mathrm{dS} = \frac{1}{2} \sum_{N_{\mathrm{j}} \in \mathcal{K}_{\mathrm{i}}} \boldsymbol{\mathcal{B}}(\overline{\mathbf{Q}}_{\mathrm{ij}}) \cdot \boldsymbol{\eta}_{\mathrm{ij}} \left(\overline{\mathbf{Q}}_{\mathrm{j}}^n - \overline{\mathbf{Q}}_{\mathrm{i}}^n\right), \qquad \overline{\mathbf{Q}}_{\mathrm{ij}} = \overline{\mathbf{Q}}_{\mathrm{i}} + \overline{\mathbf{Q}}_{\mathrm{j}}. \tag{28}$$

Meanwhile, the second term in Equation (27) corresponds to the smooth contribution of the non-conservative product within the cell, which must be taken into account to get high-order accurate schemes. To compute it, we again employ the dual grid structure and approximate the needed gradients using a Galerkin approach in the primal grid. Then, the gradient for the non-conservative product contribution is computed as a weighted average of the contribution from the two primal subtriangles composing it, i.e.,

$$\int_{C_{\mathrm{i}} \setminus \Gamma_{\mathrm{i}}} \boldsymbol{\mathcal{B}}(\overline{\mathbf{Q}}^n) \cdot \nabla \overline{\mathbf{Q}}^n \,\mathrm{dV} = |C_{\mathrm{i}}| \, \boldsymbol{\mathcal{B}}(\overline{\mathbf{Q}}_{\mathrm{i}}^n) \left(\frac{|C_{\mathrm{i}_1}|}{|C_{\mathrm{i}}|} \nabla \overline{\mathbf{Q}}_{\mathrm{i}_1}^n + \frac{|C_{\mathrm{i}_2}|}{|C_{\mathrm{i}}|} \nabla \overline{\mathbf{Q}}_{\mathrm{i}_2}^n \right), \tag{29}$$

with i_1 and i_2 the two halves of cell C_{i}, $C_{\mathrm{i}} = C_{\mathrm{i}_1} \cup C_{\mathrm{i}_2}$, $C_{\mathrm{i}_1} \subset T_{\mathrm{i}_1}$, $C_{\mathrm{i}_2} \subset T_{\mathrm{i}_2}$, $T_{\mathrm{i}_1}, T_{\mathrm{i}_2} \in \boldsymbol{\Upsilon}$, and $\nabla \overline{\mathbf{Q}}_{\mathrm{i}_1}$, $\nabla \overline{\mathbf{Q}}_{\mathrm{i}_2}$ the gradients of $\overline{\mathbf{Q}}$ computed in T_{i_1} and T_{i_2}, respectively.

3.5.4 Source term in the momentum equations

The source term of the momentum equations is integrated on each dual cell employing the density at the previous time step as

$$\int_{C_\mathrm{i}} \overline{\rho}^n \mathbf{g} \,\mathrm{dV} = |C_\mathrm{i}| \, \overline{\rho}_\mathrm{i}^n \mathbf{g}. \tag{30}$$

3.5.5 Implicit discretisation of the algebraic source terms for the distortion and heat conduction fields

The algebraic source terms related to the relaxation times may become very stiff in the fluid limit of the equations. Consequently, the needed time step to treat them explicitly may become very restrictive. To avoid this issue, an implicit discretisation of those algebraic source terms can be performed, [10]. We assume that convective and non-conservative terms in (15) have already been computed. Then, we get the following system for the algebraic source terms:

$$\frac{1}{\Delta t}\left(A_{ik}^{n+1} - A_{ik}^{*}\right) = -\frac{1}{\theta_1^{n+1}\left(\tau_1\right)} E_{A_{ik}}^{n+1}, \tag{31a}$$

$$\frac{1}{\Delta t}\left(J_{k}^{n+1} - J_{k}^{*}\right) = -\frac{1}{\theta_2^{\star}\left(\tau_2\right)} E_{J_k}^{n+1}, \tag{31b}$$

with

$$A_{ik}^{*} = A_{ik}^{n} - \frac{\partial}{\partial x_k}\left(u_m^n A_{im}^n\right) - u_j^n \frac{\partial}{\partial x_j} A_{ik}^n + u_j^n \frac{\partial}{\partial x_k} A_{ij}^n, \tag{32}$$

$$J_{k}^{*} = J_{k}^{n} - \frac{\partial}{\partial x_k}\left(J_m^n u_m^n\right) - \frac{\partial}{\partial x_k} T^n - u_j^n \left(\frac{\partial}{\partial x_j} J_k^n + \frac{\partial}{\partial x_k} J_j^n\right), \tag{33}$$

that have already been computed explicitly using the explicit finite volume scheme. We note that system (31) can also be seen as a second splitting of the original model (11) with corresponding continuous source term subsystem

$$\partial_t A_{ik} = -\frac{1}{\theta_1\left(\tau_1\right)} E_{A_{ik}}, \tag{34a}$$

$$\partial_t J_k = -\frac{1}{\theta_2\left(\tau_2\right)} E_{J_k}. \tag{34b}$$

Denoting $\mathbf{Y} = (\mathbf{A}, \mathbf{J})^T = (A_1, \ldots, A_9, J_1, \ldots, J_3)^T$ the vector of unknowns, the system (34) can be recast into an ordinary differential equation system of the form

$$\mathbf{Y}'(t) = \mathbf{g}(t, \mathbf{Y}(t)), \tag{35}$$

that can be solved using classical Runge-Kutta methods as the implicit Euler scheme or the DIRK scheme of Pareschi and Russo, [60]. This methodology requires the computation of the root of $\mathbf{G}(\mathbf{Y}(t)) = \mathbf{Y}'(t) - \mathbf{g}(t, \mathbf{Y}(t))$ which is performed using an inexact Newton algorithm, [34].

Focusing on the weakly compressible GPR system, once the distortion and thermal impulse fields are obtained at the new time step, they are used to approximate the source term contribution of the pressure equation (15f) at each cell C_{i} as

$$\int_{C_{\mathrm{i}}} \left[\frac{\rho^{n+1}\,(\gamma-1)}{\theta_1^{n+1}\,(\tau_1)} E_{A_{ik}}^{n+1} E_{A_{ik}}^{n+1} + \frac{\rho^{n+1}\,(\gamma-1)}{\theta_2^{\star}\,(\tau_2)} E_{J_k}^{n+1} E_{J_k}^{n+1} \right] \mathrm{dV} =$$

$$|C_{\mathrm{i}}| \left[\frac{3\rho_0^2 c_s^2(\gamma-1)}{\tau_1 \rho_{\mathrm{i}}^{n+1} \left|\mathbf{A}_{\mathrm{i}}^{n+1}\right|^{\frac{11}{3}}} \left(\mathbf{A}_{\mathrm{i}}^{n+1} \mathring{\mathbf{G}}_{\mathrm{i}}^{n+1}\right) \cdot \left(\mathbf{A}_{\mathrm{i}}^{n+1} \mathring{\mathbf{G}}_{\mathrm{i}}^{n+1}\right) + \frac{c_h^2(\gamma-1)\rho_{\mathrm{i}}^{n+1} T_{\mathrm{i}}^{n}}{\tau_2 \rho_0 T_0} \mathbf{J}_{\mathrm{i}} \cdot \mathbf{J}_{\mathrm{i}} \right]. \tag{36}$$

3.6 Interpolation stage

In the weakly compressible GPR model, the pressure is computed in two steps. First, an intermediate value gathering the contributions of the convective terms and non-conservative products is obtained from solving (15f) and (15g). The obtained value is then employed within the system (16) to calculate the pressure at the new time step. Hence, before the projection stage, the intermediate pressure $\widetilde{p}_p$ is interpolated from the dual cells, C_{i}, to the primal elements, $T_{\boldsymbol{\kappa}}$, as

$$\widetilde{p}_{p\,\boldsymbol{\kappa}} = \sum_{\mathrm{i}\in\mathcal{K}_{\boldsymbol{\kappa}}} \frac{|T_{\boldsymbol{\kappa}\mathrm{i}}|}{|T_{\boldsymbol{\kappa}}|} \widetilde{p}_{p\,\mathrm{i}}, \qquad T_{\boldsymbol{\kappa}\mathrm{i}} = T_{\boldsymbol{\kappa}} \cap C_{\mathrm{i}}, \tag{37}$$

with $\mathcal{K}_{\boldsymbol{\kappa}}$ the set of dual cell index identifying the dual elements generated from the primal faces of element $T_{\boldsymbol{\kappa}}$. Next, the intermediate pressure $\widetilde{p}$ is computed as

$$\widetilde{p}_{\boldsymbol{\kappa}} = \widetilde{p}_{p\,\boldsymbol{\kappa}} + \widetilde{p}_{\rho\,\boldsymbol{\kappa}}, \tag{38}$$

where the contribution of the non-conservative product on the density, $\widetilde{p}_\rho$, to the pressure equation (15g), is computed using a finite volume approach in the primal grid. More precisely, we have

$$\begin{aligned} \widetilde{p}_{\rho\,\boldsymbol{\kappa}} = -\frac{\Delta t}{|T_{\boldsymbol{\kappa}}|} \int_{T_{\boldsymbol{\kappa}}} (c^n)^2\, \mathbf{u}^n \cdot \nabla\, \rho^n \,\mathrm{dV} &= \frac{\Delta t}{|T_{\boldsymbol{\kappa}}|} \left(c_{\boldsymbol{\kappa}}^n\right)^2 \mathbf{u}_{\boldsymbol{\kappa}}^n \cdot \sum_{\mathrm{i}\in\mathcal{K}_{\boldsymbol{\kappa}}} \int_{\Gamma_{\boldsymbol{\kappa}\mathrm{i}}} \rho_{\mathrm{i}}^n \mathbf{n}_{\boldsymbol{\kappa}\mathrm{i}} \,\mathrm{dV} \\ &= \frac{\Delta t}{|T_{\boldsymbol{\kappa}}|} \left(c_{\boldsymbol{\kappa}}^n\right)^2 \mathbf{u}_{\boldsymbol{\kappa}}^n \cdot \sum_{\mathrm{i}\in\mathcal{K}_{\boldsymbol{\kappa}}} \rho_{\mathrm{i}}^n \boldsymbol{\eta}_{\boldsymbol{\kappa}\mathrm{i}}, \end{aligned} \tag{39}$$

with

$$c_{\boldsymbol{\kappa}}^n = \sum_{\mathrm{i}\in\mathcal{K}_{\boldsymbol{\kappa}}} \frac{\gamma\,|T_{\boldsymbol{\kappa}\mathrm{i}}|\,p_{\boldsymbol{\kappa}\mathrm{i}}^n}{|T_{\boldsymbol{\kappa}}|\,\rho_{\mathrm{i}}^n}, \qquad p_{\boldsymbol{\kappa}\mathrm{i}}^n = \frac{1}{2}\sum_{\mathrm{m}=1}^{2} p_{\boldsymbol{\kappa}\mathrm{i}\mathrm{m}}^n, \tag{40}$$

$p_{\boldsymbol{\kappa}\mathrm{i}\mathrm{m}}^n$ the pressure at vertex m of edge $\Gamma_{\boldsymbol{\kappa}\mathrm{i}}$, $\Gamma_{\boldsymbol{\kappa}\mathrm{i}}$ the primal edge of element $T_{\boldsymbol{\kappa}}$ used to generate C_{i}, $\mathbf{u}_{\boldsymbol{\kappa}}^n$ the velocity interpolated from the dual grid to the primal element $T_{\boldsymbol{\kappa}}$, following Equation (37), $\mathbf{n}_{\boldsymbol{\kappa}\mathrm{i}}$ the unitary outward pointing normal of $\Gamma_{\boldsymbol{\kappa}\mathrm{i}}$, and $\boldsymbol{\eta}_{\boldsymbol{\kappa}\mathrm{i}} = |\Gamma_{\boldsymbol{\kappa}\mathrm{i}}|\,\mathbf{n}_{\boldsymbol{\kappa}\mathrm{i}}$.

3.7 Projection stage. Finite element method in the primal grid

The pressure subsystem associated with the incompressible or the weakly compressible GPR models is solved by employing continuous finite element methods in the primal grid. Focusing on the weakly compressible GPR model, we substitute (14b) into (14a), obtaining

$$\frac{1}{\Delta t}\left(p^{n+1}-\widetilde{p}\right)+c^2\,\nabla\cdot\left(\rho\mathbf{u}^*\right)-c^2\Delta t\;\Delta\,p^{n+1}=0.$$

Next, multiplying the former equation by a test function $z\in V_0$,

$$V_0=\left\{z\in H^1(\Omega)\mid\int_\Omega z\,\mathrm{dV}=0\right\},$$

integrating in the computational domain Ω, and using the Green theorem, we get the weak problem

Weak problem 1 *Find $p\in V_0$ such that*

$$\frac{1}{c^2}\int_\Omega p^{n+1}z\,\mathrm{dV}+\Delta t^{\,2}\int_\Omega\nabla\,p^{n+1}\cdot\nabla\,z\,\mathrm{dV}=\frac{1}{c^2}\int_\Omega\widetilde{p}z\,\mathrm{dV}+\Delta t\int_\Omega\rho\mathbf{u}^*\cdot\nabla\,z\,\mathrm{dV}$$
$$-\Delta t\int_{\partial\Omega}\rho\mathbf{u}^{n+1}\cdot\mathbf{n}z\,\mathrm{dS}\tag{41}$$

for all $z\in V_0$.

Similarly, for the incompressible system (14), we have

Weak problem 2 *Find $\delta p^{n+1}\in V_0$ such that*

$$\int_\Omega\nabla\,\delta p^{n+1}\cdot\nabla\,z\,\mathrm{dV}=\frac{1}{\Delta t}\int_\Omega\rho\mathbf{u}^*\cdot\nabla\,z\,\mathrm{dV}-\frac{1}{\Delta t}\int_{\partial\Omega}\rho\mathbf{u}^{n+1}\cdot\mathbf{n}z\,\mathrm{dS}$$

for all $z\in V_0$.

Finally, we employ the second order $\mathbb{P}_1$ continuous finite element method to discretise the weak problems, and the resulting algebraic systems are solved using a matrix-free conjugate gradient method. Let us note that the obtained weak problems correspond to the ones arising for the incompressible and weakly compressible Navier-Stokes equations when the splitting procedure [83] is considered; further details on the applied methodology can be found in [25,4].

3.8 Correction stage

Once the new pressure has been obtained as the solution of the projection stage, the intermediate momentum is updated at each dual cell C_i using (14b) and (16b), for the incompressible GPR model and the weakly compressible GPR model, respectively. The involved pressure gradients are computed as

$$\left(\nabla\,p\right)_\mathrm{i}=\frac{1}{|T_{\boldsymbol{\kappa}}|}\sum_{\boldsymbol{\kappa}\in\mathcal{T}_\mathrm{i}}|T_{\boldsymbol{\kappa}\mathrm{i}}|\left(\nabla\,p\right)_{\boldsymbol{\kappa}},\tag{42}$$

with $\mathcal{T}_\mathrm{i}$ the set of primal elements related to C_i and $\left(\nabla\,p\right)_{\boldsymbol{\kappa}}$ calculated in the primal cells using the $\mathbb{P}_1$ finite element basis functions.

3.9 Boundary conditions

Before assessing the proposed methodology, we briefly introduce the main types of boundary conditions employed in Section 4.

If a periodic solution is expected, we may simply employ periodic boundary conditions, which are implemented assuming each pair of boundaries to have a periodic mesh. Consequently, the vertex of the primal elements where the pressure is computed can be merged. On the other hand, we defined each couple of dual elements related through the boundary as a unique dual cell for the dual grid. Then, the solution at the boundary cells is computed as if they were interior elements.

Regarding Dirichlet boundary conditions, two different subcases are considered: strong and weak boundary conditions. If strong boundary conditions are selected, the values of the conservative variables are directly imposed as the solution in the boundary cells. Alternatively, weakly Dirichlet boundary conditions assume the exact solution to be located at the boundary. Hence, the fluxes and gradients needed to compute the explicit stage are approximated by setting the given values in the neighbouring ghost cells. For both kinds of boundary conditions, we can further set the pressure as a Dirichlet boundary condition by defining its values at the boundary vertex. Nevertheless, in most cases, we simply employ Neumann boundary conditions for the pressure field.

Focusing on the fluid limit of the model and considering the presence of walls, the velocity and pressure fields at the boundary cells are computed as for a Navier-Stokes solver, see e.g. [26]. Nevertheless, special care must be paid to approximating the distortion field, which is left "free" at the boundary. So, a specific approach to compute the distortion field at the neighbouring of the wall is required. We first rewrite the distortion field equations as

$$\frac{1}{\Delta t}\left(A_{ik}^{n+1}-A_{ik}^{n}\right)+A_{im}^{n}\frac{\partial}{\partial x_k}u_m^n+u_m^n\frac{\partial}{\partial x_m}A_{ik}^{n}=-\frac{1}{\theta_1^{n+1}(\tau_1)}E_{A_{ik}}^{n+1}, \tag{43}$$

which corresponds to an asymptotic preserving scheme in the fluid relaxation limit of the equations, i.e., as $\tau_1 \to 0$ we recover the Navier-Stokes equations, [14]. Further, this allows the flux and the non-conservative product contributions to be reordered into two terms. The first one is linear with respect to the distortion field, $\mathbf{A}\cdot\nabla\mathbf{u}$, and is simply discretised using the gradients obtained at the dual cells applying the Galerkin approach, i.e., as introduced for the smooth part of the non-conservative products (29). Meanwhile, for the second term, $\mathbf{u}\nabla\mathbf{A}$, the path conservative methodology proposed in Section 3.5.3 is employed. Then, the term $\mathbf{A}\cdot\nabla\mathbf{u}$ can be treated implicitly by including it within the source term system. Consequently, the explicit stage of the algorithm neglects the presence of this term. Then, instead of solving (31) for the distortion field, at the wall boundary cells, we have the implicit system

$$A_{ik}^{n+1}+\frac{\Delta t}{\theta_1^{n+1}(\tau_1)}E_{A_{ik}}^{n+1}=A_{ik}^{\star}, \tag{44a}$$

$$A_{ik}^{\star}=A_{ik}^{n}-\Delta t\,A_{im}^{n}\frac{\partial}{\partial x_k}\tilde{u}_m-\Delta t\,u_m^n\frac{\partial}{\partial x_m}A_{ik}^{n}, \tag{44b}$$

with the velocity gradients, $\nabla\tilde{\mathbf{u}}$, approximated using the Galerkin approach by setting the known velocity at the Crouzeix-Raviart node located at the boundary

and the previous time step velocity values at the internal nodes. Let us remark that the use of (43) for the distortion field computation instead of the original version in terms of a convective flux term, (13b), leads to an asymptotic preserving scheme in the fluid limit of the model, further details can be found in [14].

3.10 Parallel implementation

The code has been parallelized using the Message-Passing-Interface (MPI) standard, [45], enabling simulations involving millions of degrees of freedom through domain decomposition. In this approach, each CPU handles computations within its assigned subdomain and exchanges necessary data with neighboring CPUs. The scalability of the developed algorithm is primarily conditioned by its hybrid character. Hence, the same challenges and advantages on parallelization are observed when applying the proposed hybrid method to the compressible Navier-Stokes equations and to the GPR model, being the greater number of equations solved in the explicit stage of the GPR model the only difference.

To illustrate the advantages of parallelization in the family of hybrid methods, a scalability study is conducted using the Taylor-Green vortex (TGV) benchmark in a two-dimensional domain $\Omega = [0, 2\pi]^2$ (see Section 4.1 for further details on the test setup). A strong scaling test is performed by fixing the problem size and measuring the wall clock time for both sequential and parallel simulations. The speedup $S(p)$ and the efficiency $E(p)$ are defined as:

$$S(p) = \frac{T_{\text{serial}}}{T_{\text{parallel}}(p)}, \qquad E(p) = \frac{S(p)}{p} = \frac{T_{\text{serial}}}{p\, T_{\text{parallel}}(p)}, \tag{45}$$

where $T_{\text{parallel}}(p)$ is the execution time required by p processors, and T_{serial} is the execution time of the sequential code. Ideally, the speedup is equal to the number of processors, resulting in linear speedup with $S(p) = p$, and every processor contributes 100% of its computational power.

All simulations in the scaling study were performed on an Intel(R) Xeon(R) Gold 6252N CPU @ 2.30GHz. For reliable performance metrics, each simulation was executed 10 times, and the average runtime was used to compute speedup and efficiency.

Figure 2 illustrates the strong scaling results for the TGV benchmark. The left plot shows the speedup computed using (45) compared to the ideal speedup from 1 to 96 processors. The right plot displays the efficiency calculated by using (45). Even thought these simulations have been performed without any code optimization, the achieved efficiency is around 65%. The main performance bottleneck occurs in the solution of the pressure system, which relies on the conjugate gradient method. This method requires data communication between the CPUs in each iteration to evaluate the residual tolerance, leading to the well-documented scalability limitation of this type of problems. In contrast, the explicit stage of the algorithm exhibits good scalability, since each CPU independently computes the intermediate values for the variables, after exchanging data with its neighbours over a limited number of cells adjacent to the partition interface. Finally, the implicit system for the source terms is local, so no information exchange between CPUs is required. Further details on the parallelization of hybrid methods, particularly for the Navier-Stokes and shallow water equations, can be found in [67].

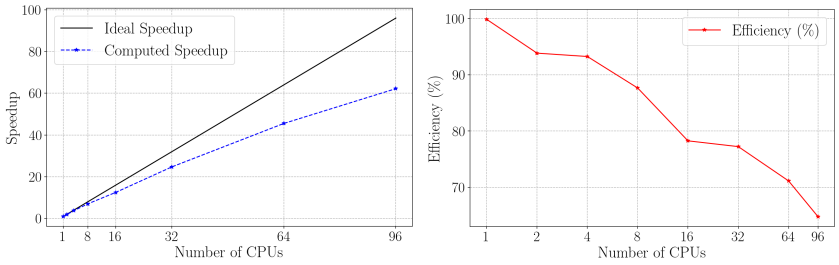

Fig. 2 Left: Computed speedup compared with the ideal speedup. Right: Efficiency as a function of processor count. In both cases, the number of processors was from 1 to 96.

4 Numerical results

In this section, we assess the proposed methodology through classical test problems for incompressible and weakly compressible flows. The test cases are described employing the international system of units. Besides, unless stated contrary, all test cases are run with a variable time-stepping attending to a CFL $= 0.5$ so that stability of the explicit part of the scheme is guaranteed. Taking into account that the pressure subsystem and the source terms for the distortion, thermal impulse and pressure equations are treated implicitly, the time step restriction only depends on the explicit transport stage and reads

$$\Delta t = \min_{C_\mathrm{i}} \{\Delta t_\mathrm{i}\}, \qquad \Delta t_\mathrm{i} = \frac{\mathrm{CFL}\, r_\mathrm{i}}{|\lambda_\mathrm{i}|_{\max}},$$

with r_i the incircle diameter of C_i and $|\lambda_\mathrm{i}|_{\max}$ the maximum absolute eigenvalue associated with the explicit subsystem. The eigenvalues of the transport subsystem for the 2D and 3D cases are approximated from the ones computed in the 1D case, which correspond to:

$$\lambda \in \left\{ \frac{3}{2}|\mathbf{u}| - c, |\mathbf{u}|, \frac{3}{2}|\mathbf{u}| + c \right\},$$

where c is defined as in (21) for the incompressible GPR model, and as in (22) for the weakly compressible one.

4.1 Convergence study: Taylor-Green Vortex

As a first test case, we consider the 2D Taylor-Green vortex benchmark whose known exact solution for the Euler equations in $\Omega = [0, 2\pi]^2$ is given by

$$u(\mathbf{x}, t) = \begin{pmatrix} \sin(x)\cos(y) \\ -\cos(x)\sin(y) \end{pmatrix}, \quad p(\mathbf{x}, t) = \frac{p_0}{\gamma} + \frac{1}{4}(\cos(2x) + \cos(2y)).$$

We run a set of simulations for the successively refined triangular grids described in Table 1 with both the first and second order approaches for the convective terms using the incompressible and weakly compressible GPR models. In particular, in the incompressible regime, we simply set $p_0 = 0$, and the model parameters are

$c_s = 0$ and $\mu = 0$. Meanwhile, to test the weakly compressible code, we take $p_0 = 10^5$, $\gamma = 1.4$, $c_v = 2.5$, $c_s = c_h = 0$, and $\mu = \kappa = 0$, yielding a characteristic Mach number of $M \approx 3.2 \cdot 10^{-3}$. In all cases, the expected convergence orders are attained, as shown in Tables 2-3.

Mesh	Elements	Vertices	Dual elements
M_1	128	81	208
M_2	512	289	800
M_3	2048	1089	3136
M_4	8192	4225	12416
M_5	32768	16641	49408
M_6	131072	66049	197120

Table 1 2D Taylor-Green vortex. Main features of the primal triangular grids used to run the convergence table.

Mesh	First order scheme				Local ADER scheme			
	$L^2_\Omega(\mathbf{u})$	$\mathcal{O}(\mathbf{u})$	$L^2_\Omega(p)$	$\mathcal{O}(p)$	$L^2_\Omega(\mathbf{u})$	$\mathcal{O}(\mathbf{u})$	$L^2_\Omega(p)$	$\mathcal{O}(p)$
M1	$3.45 \cdot 10^{-1}$		$7.42 \cdot 10^{-1}$		$1.23 \cdot 10^{-1}$		$4.21 \cdot 10^{-1}$	
M2	$1.99 \cdot 10^{-1}$	0.79	$2.02 \cdot 10^{-1}$	1.88	$3.06 \cdot 10^{-2}$	2.01	$2.11 \cdot 10^{-1}$	1.00
M3	$1.09 \cdot 10^{-1}$	0.87	$9.44 \cdot 10^{-2}$	1.10	$7.62 \cdot 10^{-3}$	2.01	$6.35 \cdot 10^{-2}$	1.73
M4	$5.71 \cdot 10^{-2}$	0.93	$4.64 \cdot 10^{-2}$	1.03	$1.90 \cdot 10^{-3}$	2.00	$1.66 \cdot 10^{-2}$	1.93
M5	$2.93 \cdot 10^{-2}$	0.97	$2.31 \cdot 10^{-2}$	1.01	$4.75 \cdot 10^{-4}$	2.00	$4.21 \cdot 10^{-3}$	1.98
M6	$1.48 \cdot 10^{-2}$	0.98	$1.15 \cdot 10^{-2}$	1.00	$1.19 \cdot 10^{-4}$	2.00	$1.06 \cdot 10^{-3}$	1.99
M7	$7.46 \cdot 10^{-3}$	0.99	$5.75 \cdot 10^{-3}$	1.00	$2.97 \cdot 10^{-5}$	2.00	$2.64 \cdot 10^{-4}$	2.00

Table 2 2D Taylor-Green vortex. Incompressible GPR model. Spatial L_2 error norms and convergence rates at time $t = 0.1$.

Mesh	Local ADER scheme					
	$L^2_\Omega(\rho)$	$\mathcal{O}(\rho)$	$L^2_\Omega(\mathbf{u})$	$\mathcal{O}(\mathbf{u})$	$L^2_\Omega(p)$	$\mathcal{O}(p)$
M1	$2.30 \cdot 10^{-2}$		$1.04 \cdot 10^{-1}$		$9.40 \cdot 10^{1}$	
M2	$3.23 \cdot 10^{-3}$	2.83	$2.94 \cdot 10^{-2}$	1.82	$1.55 \cdot 10^{1}$	2.60
M3	$4.54 \cdot 10^{-4}$	2.83	$7.62 \cdot 10^{-3}$	1.95	$1.78 \cdot 10^{0}$	3.12
M4	$7.71 \cdot 10^{-5}$	2.56	$1.90 \cdot 10^{-3}$	2.00	$1.74 \cdot 10^{-1}$	3.35
M5	$1.63 \cdot 10^{-5}$	2.24	$4.75 \cdot 10^{-4}$	2.00	$1.67 \cdot 10^{-2}$	3.38
M6	$4.00 \cdot 10^{-6}$	2.02	$1.19 \cdot 10^{-4}$	2.00	$1.71 \cdot 10^{-3}$	3.29

Table 3 2D Taylor-Green vortex. Weakly compressible GPR model. Spatial L_2 error norms and convergence rates at time $t = 0.1$.

The Taylor-Green vortex benchmark is also employed to numerically analyse the asymptotic preserving property of the hybrid approach in the incompressible limit. To this end a set of simulations for $M \in \left\{10^{-3}, 10^{-4}, 10^{-5}, 10^{-6}\right\}$ is run

employing the second order scheme with $p_0 \in \{10^6, 10^8, 10^{10}, 10^{12}\}$, respectively. Due to the large magnitude of the pressure, we have set quadruple precision arithmetic for $M = 10^{-5}$ and $M = 10^{-6}$. In Table 4, we observe that second order of accuracy is reached independently of the Mach number. Further, the magnitude of the errors for the density and velocity fields is maintained as $M \to 0$. Consequently, even if not verifying the AP property strictly, for which the errors should diminish quadratically with M, the proposed scheme overcomes one shortcoming of many classical schemes that are not always able to attain the expected order of accuracy when addressing very low Mach number regimes.

Mesh	$L^2_\Omega(\rho)$	$\mathcal{O}(\rho)$	$L^2_\Omega(\nabla\cdot\mathbf{u})$	$\mathcal{O}(\nabla\cdot\mathbf{u})$	$L^2_\Omega(\mathbf{u})$	$\mathcal{O}(\mathbf{u})$	$L^2_\Omega(p)$	$\mathcal{O}(p)$
$M = 10^{-3}$ (double precision)								
M1	$2.30 \cdot 10^{-2}$		$3.85 \cdot 10^{-1}$		$1.04 \cdot 10^{-1}$		$9.40 \cdot 10^{2}$	
M2	$3.23 \cdot 10^{-3}$	2.83	$9.34 \cdot 10^{-2}$	2.04	$2.94 \cdot 10^{-2}$	1.82	$1.55 \cdot 10^{2}$	2.60
M3	$4.54 \cdot 10^{-4}$	2.83	$2.36 \cdot 10^{-2}$	1.98	$7.62 \cdot 10^{-3}$	1.95	$1.78 \cdot 10^{1}$	3.12
M4	$7.72 \cdot 10^{-5}$	2.56	$5.99 \cdot 10^{-3}$	1.98	$1.90 \cdot 10^{-3}$	2.00	$1.74 \cdot 10^{0}$	3.35
M5	$1.63 \cdot 10^{-5}$	2.25	$1.50 \cdot 10^{-3}$	1.99	$4.75 \cdot 10^{-4}$	2.00	$1.66 \cdot 10^{-1}$	3.39
$M = 10^{-4}$ (double precision)								
M1	$2.30 \cdot 10^{-2}$		$3.85 \cdot 10^{-1}$		$1.04 \cdot 10^{-1}$		$9.40 \cdot 10^{4}$	
M2	$3.23 \cdot 10^{-3}$	2.83	$9.34 \cdot 10^{-2}$	2.04	$2.94 \cdot 10^{-2}$	1.82	$1.55 \cdot 10^{4}$	2.60
M3	$4.54 \cdot 10^{-4}$	2.83	$2.36 \cdot 10^{-2}$	1.98	$7.62 \cdot 10^{-3}$	1.95	$1.78 \cdot 10^{3}$	3.12
M4	$7.72 \cdot 10^{-5}$	2.56	$5.99 \cdot 10^{-3}$	1.98	$1.90 \cdot 10^{-3}$	2.00	$1.74 \cdot 10^{2}$	3.35
M5	$1.63 \cdot 10^{-5}$	2.25	$1.50 \cdot 10^{-3}$	1.99	$4.75 \cdot 10^{-4}$	2.00	$1.65 \cdot 10^{1}$	3.39
$M = 10^{-5}$ (quadruple precision)								
M1	$2.30 \cdot 10^{-2}$		$3.85 \cdot 10^{-1}$		$1.04 \cdot 10^{-1}$		$9.40 \cdot 10^{6}$	
M2	$3.23 \cdot 10^{-3}$	2.83	$9.34 \cdot 10^{-2}$	2.04	$2.94 \cdot 10^{-2}$	1.82	$1.55 \cdot 10^{6}$	2.60
M3	$4.54 \cdot 10^{-4}$	2.83	$2.36 \cdot 10^{-2}$	1.98	$7.62 \cdot 10^{-3}$	1.95	$1.78 \cdot 10^{5}$	3.13
M4	$7.72 \cdot 10^{-5}$	2.56	$5.99 \cdot 10^{-3}$	1.98	$1.90 \cdot 10^{-3}$	2.00	$1.66 \cdot 10^{4}$	3.42
M5	$1.63 \cdot 10^{-5}$	2.25	$1.50 \cdot 10^{-3}$	1.99	$4.75 \cdot 10^{-4}$	2.00	$1.66 \cdot 10^{3}$	3.32
$M = 10^{-6}$ (quadruple precision)								
M1	$2.30 \cdot 10^{-2}$		$3.85 \cdot 10^{-1}$		$1.04 \cdot 10^{-1}$		$9.40 \cdot 10^{8}$	
M2	$3.23 \cdot 10^{-3}$	2.83	$9.33 \cdot 10^{-2}$	2.05	$2.94 \cdot 10^{-2}$	1.82	$1.55 \cdot 10^{8}$	2.60
M3	$4.54 \cdot 10^{-4}$	2.83	$2.36 \cdot 10^{-2}$	1.98	$7.62 \cdot 10^{-3}$	1.95	$1.78 \cdot 10^{7}$	3.12
M4	$7.72 \cdot 10^{-5}$	2.56	$5.99 \cdot 10^{-3}$	1.98	$1.90 \cdot 10^{-3}$	2.00	$1.74 \cdot 10^{6}$	3.35
M5	$1.63 \cdot 10^{-5}$	2.24	$1.50 \cdot 10^{-3}$	1.99	$4.75 \cdot 10^{-4}$	2.00	$1.66 \cdot 10^{5}$	3.39

Table 4 2D Taylor-Green vortex. Spatial L_2 error norms and convergence rates at time $t = 0.1$ for $M \in \{10^{-3}, 10^{-4}, 10^{-5}, 10^{-6}\}$. Results computed using the second order approach.

4.2 Lid-driven cavity

To analyse the behaviour of the proposed methodology in the incompressible fluid limit, we study the lid-driven cavity benchmark, [47]. We consider an initial fluid at rest with $\mathbf{u} = \mathbf{0}$, $p = \rho = 1$, $\mathbf{A} = \mathbf{I}$, $c_s = 8$, and $\mu = 10^{-2}$. Homogeneous wall boundary conditions are set in the bottom and laterals of the computational domain $\Omega = [-0.5, 0.5]^2$, while the upper bound is assumed to be moving horizontally with a lid velocity $u_{\text{lid}} = 1$. The new hybrid FV/FE methodology is employed

to solve the incompressible GPR model up to time $t = 10$. The obtained results are depicted in Figure 3. We can observe a good qualitative agreement with former results available in the bibliography, see, e.g. [22]. Moreover, Figure 3 also reports the 1D cuts of the velocity field along the horizontal and vertical centerlines of the domain, which compare well with the reference data in [47].

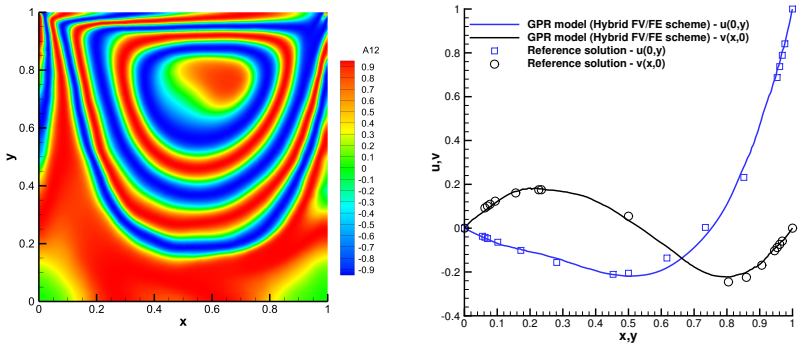

Fig. 3 Lid-driven cavity. Left: contour plot of the distortion component A_{12}. Right: 1D cut in $x-$ and $y-$directions of the velocity components u_2 and u_1 computed using the new hybrid FV/FE method for the incompressible GPR model (blue solid line - u_1 and dark grey solid line - u_2) and reference solutions reported in [47] (blue squares - u_1 and black circles - u_2).

4.3 Shear motion

We now study four shear motion tests in the computational domain $\Omega = [-0.5, 0.5] \times [-0.05, 0.05]$ with the initial condition

$$\rho\left(\mathbf{x},0\right)=1, \quad p\left(\mathbf{x},0\right)=\frac{1}{\gamma}, \quad u_1\left(\mathbf{x},0\right)=0, \quad u_2\left(\mathbf{x},0\right)=\begin{cases}-0.1 & \text{if } y\leq 0,\\ 0.1 & \text{if } y>0,\end{cases}$$
$$\mathbf{A}\left(\mathbf{x},0\right)=\mathbf{I}, \quad \mathbf{J}=\mathbf{0}.$$

Taking the incompressible fluid limit of the GPR model by setting $c_s = c_h = 1$, $c_v = 2.5$, $\mu \in \left\{10^{-4}, 10^{-3}, 10^{-2}\right\}$, and $\kappa = \mu$, we recover the well-known first problem of Stokes with a known exact analytical solution for the incompressible Navier-Stokes equations given by

$$u_2\left(\mathbf{x},t\right)=\frac{1}{10}\text{erf}\left(\frac{x}{2\sqrt{\mu t}}\right).$$

Since these test cases are run in a 2D domain, we set periodic boundary conditions in the y-direction while strong Dirichlet boundary conditions are imposed in the left and right boundaries. A primal triangular grid of $N_x = 200$ divisions is employed for $\mu = 10^{-2}$ and $\mu = 10^{-3}$, while $N_x = 400$ is defined for $\mu = 10^{-4}$. The results obtained at time $t = 0.4$ using the hybrid FV/FE scheme with the local ADER-ENO approach for the convective terms are reported in Figure 4. Excellent agreement is observed regarding the exact solutions for the three viscosities considered.

As the fourth shear motion test, we set $\tau_1 = \tau_2 = 10^{20}$ to obtain a 1D shear solid benchmark. Then, the GPR model is solved on a triangular grid of $N_x = 400$ divisions along the x-direction. The obtained 1D cut along the centerline of the domain for the velocity component u_2 is depicted in Figure 4. We observe a good agreement with the reference solution computed employing a second order MUSCL-Hancock TVD-FV scheme on a one-dimensional grid of 1000 control volumes.

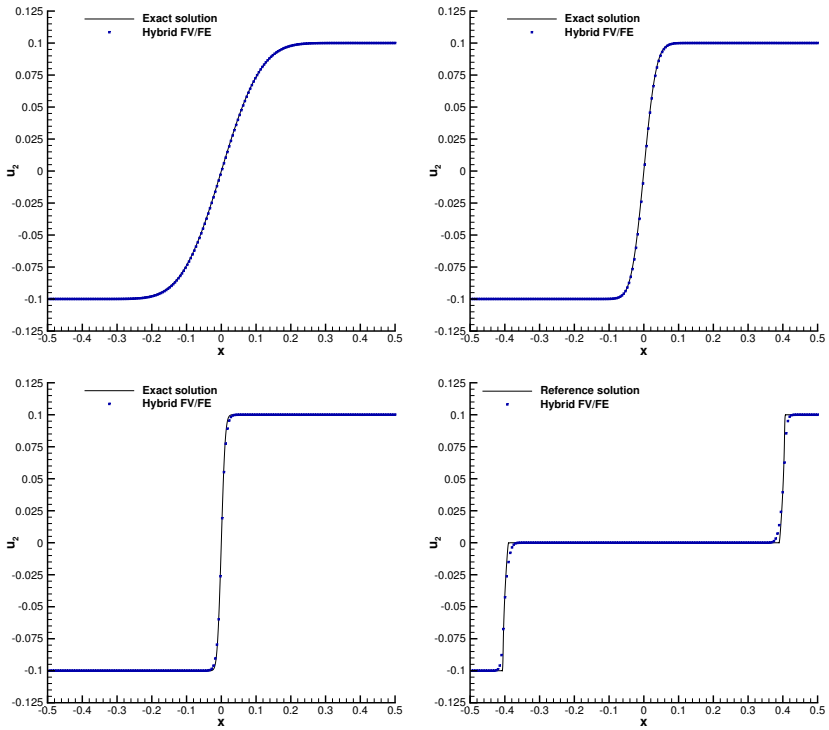

Fig. 4 Shear motion. 1D cut in the $x-$direction of the velocity component u_2 of the numerical solution obtained using the hybrid FV/FE method for the weakly compressible GPR model with the local ADER-ENO approach (blue squares). Reference solution computed with a TVD-FV scheme on a mesh of 1000 cells (black solid line). From left top to right bottom: first Stokes with $\mu = 10^{-2}$, first Stokes with $\mu = 10^{-3}$, first Stokes with $\mu = 10^{-4}$, shear solid.

4.4 Double shear layer

As the fourth test case, we consider the double shear layer benchmark whose initial condition, defined in $\Omega = [0,1]^2$, reads

$$\rho(\mathbf{x},0) = 1, \quad u_1(\mathbf{x},0) = \begin{cases} \tanh(\tilde{\rho}(y-0.25)) \text{ if } y \leq 0.5, \\ \tanh(\tilde{\rho}(0.75-y)) \text{ if } y > 0.5, \end{cases} \quad u_2(\mathbf{x},0) = \delta \sin(2\pi x),$$
$$p(\mathbf{x},0) = 0, \qquad \mathbf{A}(\mathbf{x},0) = \mathbf{I}, \qquad \mathbf{J}(\mathbf{x},0) = \mathbf{0}, \qquad \delta = 0.05, \qquad \tilde{\rho} = 30.$$

The numerical solution is computed using both the incompressible and the weakly compressible GPR methodologies with parameters $\mu = 2 \cdot 10^{-3}$, $\kappa = 4 \cdot 10^{-2}$, $c_v = 2.5$, $c_h = 2$ and $c_s = 8$. Further, the CFL is set to 0.1. Periodic boundary conditions are defined everywhere, and a computational grid formed by 2097152 primal triangular elements is considered. Figure 5 shows the contour plots of the distortion field component A_{12} at times $t \in \{0.4, 0.8, 1.2, 1.8\}$. The method captures well the very thin structures reported in the literature, e.g. [39,21] where high order explicit finite volume methods and thermodynamically compatible schemes have been used, respectively.

4.5 Solid rotor

We now consider the solid rotor test case to analyse further the behaviour of the proposed methodology in the GPR model's solid limit, [14]. The initial condition

$$\rho(\mathbf{x},0) = 1, \quad \mathbf{u}(\mathbf{x},0) = \begin{cases} \left(\frac{-y}{0.2}, \frac{x}{0.2}, 0\right)^T & \text{if } \|\mathbf{x}\| \leq 0.2, \\ \mathbf{0} & \text{if } \|\mathbf{x}\| > 0.2, \end{cases}$$
$$p(\mathbf{x},0) = 1, \quad \mathbf{A}(\mathbf{x},0) = \mathbf{I}, \quad \mathbf{J}(\mathbf{x},0) = \mathbf{0}.$$

is defined in the computational domain $\Omega = [-1,1]^2$. Moreover, the model parameters are $\tau_1 = \tau_2 = 10^{20}$, $\mu = \kappa = 0$, and $c_s = c_h = c_v = 1.0$. In Figure 6, we show the solution obtained with the hybrid FV/FE weakly compressible GPR scheme at time $t = 0.3$ employing the local ADER min-mod approach on an unstructured grid with 2975744 primal triangular elements. The provided reference solution has been obtained using the thermodynamically compatible finite volume scheme presented in [21], which solves the entropy-based formulation of the model. For comparison, the 1D profiles of the density, velocity, pressure, A_{12} and J_1 fields along $y = 0$ are reported in Figure 7. A good agreement is observed for all the schemes presented, namely the hybrid FV/FE approach, the HTC-FV scheme in [21], the HTC-DG I and HTC-DG-II methods with $N = 5$ in [22] and a second order MUSCL-Hanchock FV approach run on a very fine grid, [81].

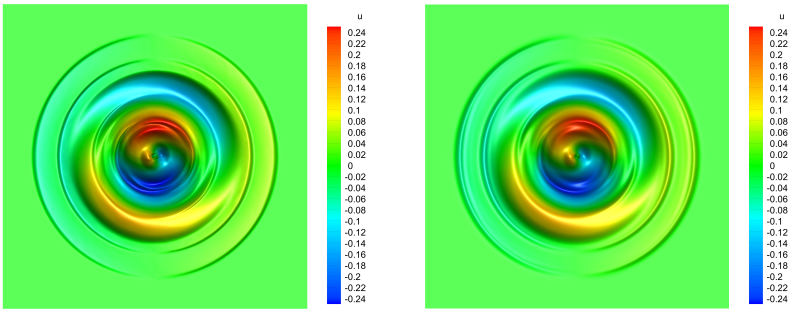

Fig. 6 Solid rotor. Contour plots of the velocity field component u_1 obtained with the hybrid FV/FE approach (left) and the HTC-FV scheme in [21] (right).

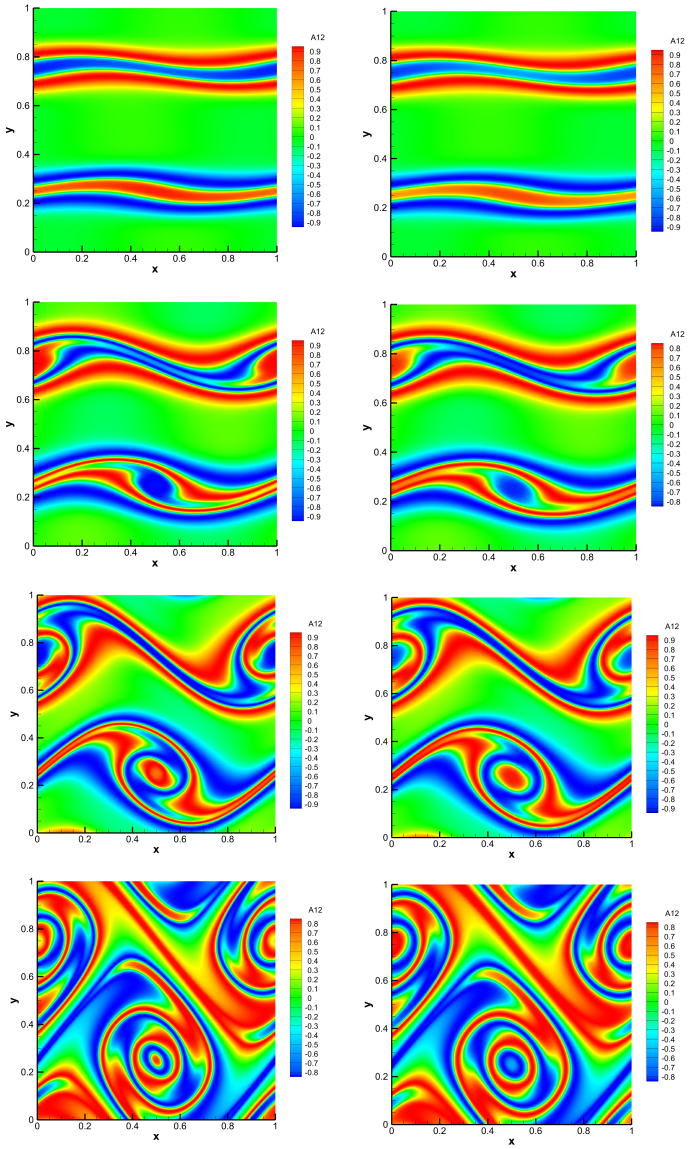

Fig. 5 Double shear layer. Contour plots of the distortion field component A_{12} obtained with the new semi-implicit hybrid FV/FE solver at times $t \in \{0.4, 0.8, 1.2, 1.8\}$ (from top to bottom). Numerical results were obtained with the incompressible GPR (left) and the weakly compressible GPR (right).

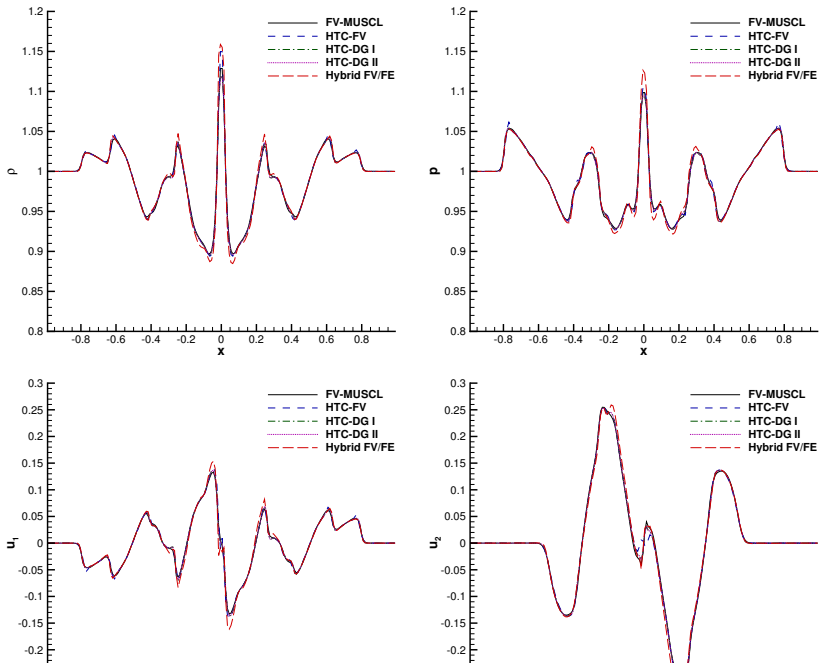

4.6 Riemann problems

The behaviour of the proposed methodology in presence of strong waves including shocks is analysed through a set of Riemann problems. We consider the computational domain $\Omega = [-0.5, 0.5] \times [-0.05, 0.05]$ and the initial conditions given by

$$\mathbf{V}(\mathbf{x}, 0) = \begin{cases} \mathbf{V}^L \text{ if } x \leq x_c, \\ \mathbf{V}^R \text{ if } x > x_c, \end{cases}$$

with the left and right states for the velocity, density and pressure fields defined in Table 5 and $\mathbf{A}_L = \mathbf{A}_R = \mathbf{I}$, $\mathbf{J}_L = \mathbf{J}_R = \mathbf{0}$. The parameters of the weakly compressible GPR model are set to $c_s = c_h = 0$ and $\mu = \kappa = 0$ for the three classical Riemann problems of the Navier-Stokes equations: RP1, RP2 and RP3. In RP4, a weak viscous fluid with shear is considered by defining $\mu = \kappa = 10^{-5}$ and $c_s = c_h = 1$. On the other hand, Riemann problems RP5 and RP6 correspond to the solid limit of the equations so $\tau_1 = \tau_2 = 10^{20}$, and we consider $c_s = 1.0$, $c_v = 2.5$. Moreover, heat conduction effects are neglected in RP5 by taking $c_h = 0$, while $c_h = 1$ is set for RP6.

Figures 8, 9 and 10 report the 1D cuts of the density, first component of the velocity vector and pressure along $y = 0$ for RP1, RP2 and RP3. A good agreement is observed with the known exact solution of the 1D compressible Euler equations, [81].

Test	ρ^L	ρ^R	u_1^L	u_1^R	u_2^L	u_2^R	p^L	p^R	x_c	t_{end}	N_x
RP1	1	0.125	0	0	0	0	1	0.1	0	0.2	400
RP2	1	1	−1	1	0	0	0.4	0.4	0	0.15	400
RP3	1	0.125	0.5	0	0	0	1	1	0	0.1	400
RP4	1	0.5	0	0	−0.2	0.2	1	0.5	0	0.2	400
RP5	1	0.5	0	0	−0.2	0.2	1	0.5	0	0.2	400
RP6	1	0.5	0	0	−0.2	0.2	1	0.5	0	0.2	400

Table 5 Riemann problems. Initial condition, location of the initial discontinuity, x_c, final time, t_{end}, and number of mesh divisions on x-direction, N_x.

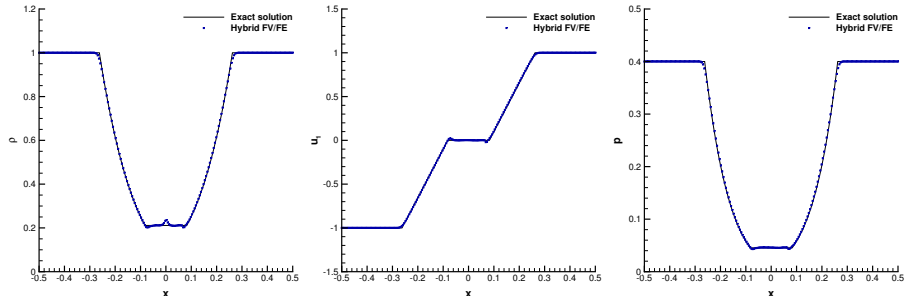

Fig. 9 RP2 double rarefaction. 1D cut in $x-$direction of the numerical solution obtained using the hybrid FV/FE method for the weakly compressible GPR model with the local ADER-BJ approach and auxiliary artificial viscosity $c_\alpha = 0.1$ (blue squares). Exact solution for the compressible Euler equations (black solid line). From left to right: density, velocity component u_1, and pressure fields.

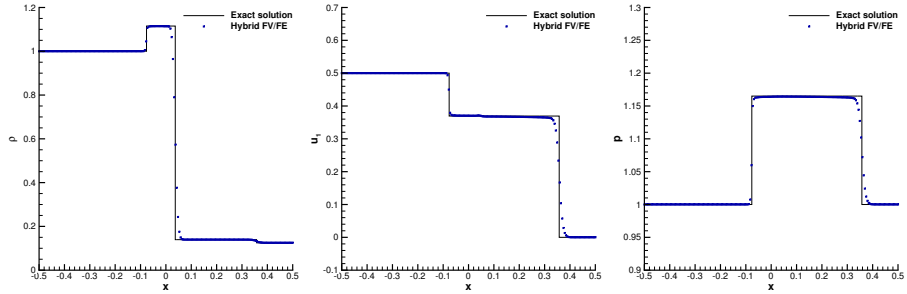

Fig. 10 RP3. 1D cut in $x-$direction of the numerical solution obtained using the hybrid FV/FE method for the weakly compressible GPR model with the local ADER-BJ approach and auxiliary artificial viscosity $c_\alpha = 0.2$ (blue squares). Exact solution for the compressible Euler equations (black solid line). From left to right: density, velocity component u_1, and pressure fields.

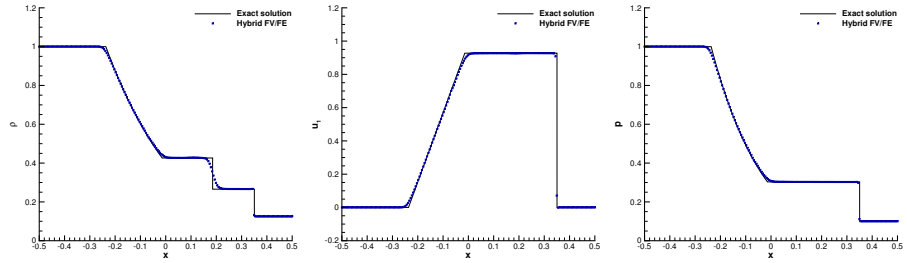

Fig. 8 RP1 Sod. 1D cut in $x-$direction of the numerical solution obtained using the hybrid FV/FE method for the weakly compressible GPR model with the local ADER-BJ approach and auxiliary artificial viscosity $c_\alpha = 0.2$ (blue squares). Exact solution for the compressible Euler equations (black solid line). From left to right: density, velocity component u_1, and pressure fields.

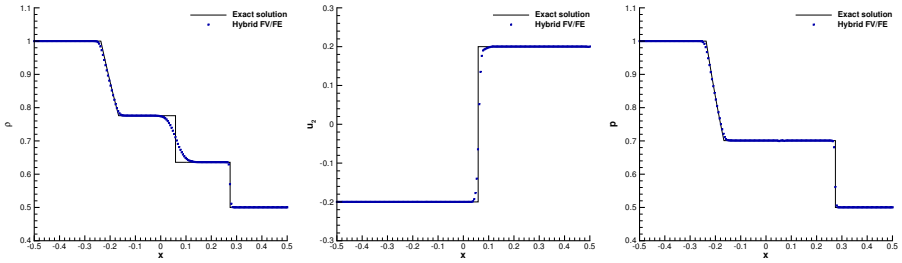

Fig. 11 RP4. 1D cut in $x-$direction of the numerical solution obtained using the hybrid FV/FE method for the weakly compressible GPR model with the local ADER-BJ approach and auxiliary artificial viscosity $c_\alpha = 1$ (blue squares). Reference solution computed with a TVD-FV scheme on a mesh of 128000 cells (black solid line). From left to right: density, velocity component u_2, and pressure fields.

RP4, RP5 and RP6 are tests specifically designed to assess the complete GPR model and are characterised by having the same initial conditions but considering different types of materials, [14]. As observed in Figure 11, the ideal fluid studied in RP4 leads to one contact discontinuity, one shear wave and two acoustic waves. The obtained results agree well with the solution computed employing a second order TVD finite volume scheme on a 1D mesh formed by 128000 cells. On the other hand, for an ideal elastic solid without heat conduction, we obtain two acoustic waves (a left rarefaction and a right shock), two shear waves (one left and one right going) and one contact discontinuity. The obtained results are compared in Figure 12 against a reference numerical solution computed in a 1D grid of 25000 cells with a second order finite volume thermodynamically compatible scheme for the entropy-based formulation of the GPR model, i.e., the scheme solves the entropy equation instead of the total energy, see [21] for more details. Finally, Figure 13 shows the results obtained for RP5, where the effect of the thermal impulse is taken into account and, as a consequence, a couple of new left and right thermo-acoustic waves arise. Also, in this case, the TVD-FV scheme for the compressible GPR model is employed to provide a reference solution.

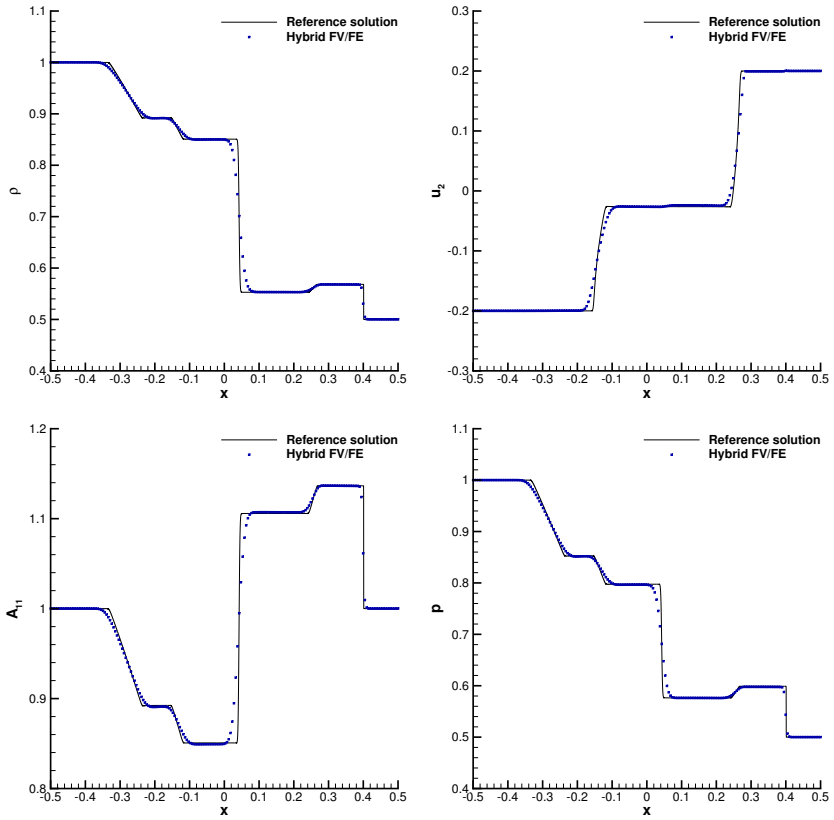

Fig. 12 RP5. 1D cut in $x-$direction of the numerical solution obtained using the hybrid FV/FE method for the weakly compressible GPR model with the local ADER-MM approach and auxiliary artificial viscosity $c_\alpha = 1$ (blue squares). Reference solution computed with an HTC-FV scheme on a mesh of 25000 cells (black solid line). From left top to right bottom: density, velocity component u_2, distortion field component A_{11}, and pressure fields.

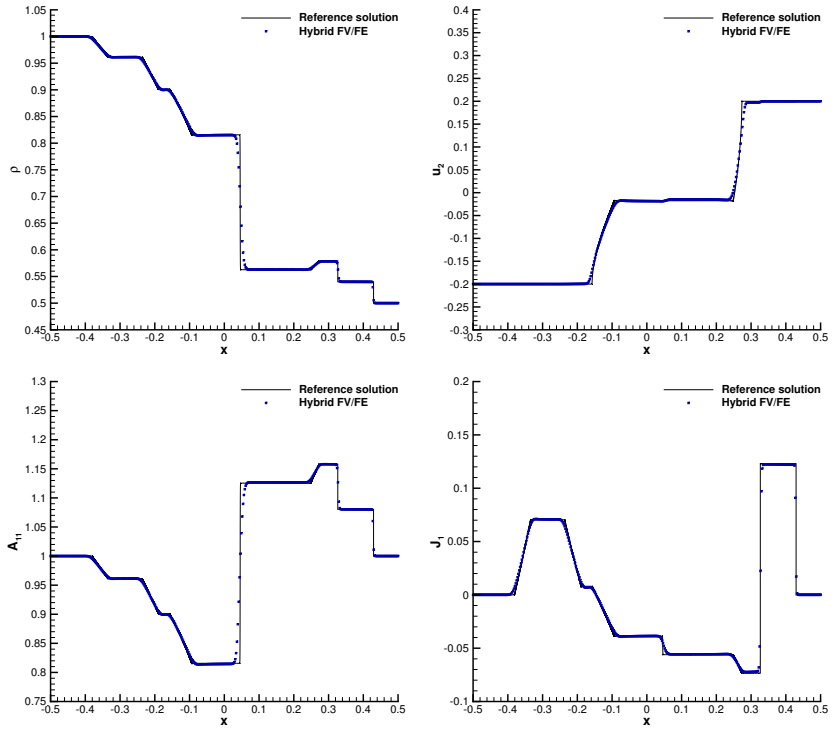

Fig. 13 RP6. 1D cut in $x-$direction of the numerical solution obtained using the hybrid FV/FE method for the weakly compressible GPR model with the local ADER-MM approach and auxiliary artificial viscosity $c_\alpha = 1$ (blue squares). Reference solution computed with an HTC-FV scheme on a mesh of 25000 cells (black solid line). From left top to right bottom: density, velocity component u_2, distortion field component A_{11}, and thermal impulse component J_1 fields.

4.7 2D circular explosions

We now address two circular explosion problems, one in the fluid framework and the other one in the solid limit of the weakly compressible GPR model.

4.7.1 Fluid circular explosion

First, we consider the classical circular explosion problem based on the extension to radial flows of the 1D Sod shock tube benchmark, [13], and whose initial condition is given by

$$\rho(\mathbf{x},0) = \begin{cases} 1 & \text{if } r \leq 0.5, \\ 0.125 & \text{if } r > 0.5, \end{cases} \qquad \mathbf{u}(\mathbf{x},0) = \mathbf{0}, \qquad p(\mathbf{x},0) = \begin{cases} 1 & \text{if } r \leq 0.5, \\ 0.1 & \text{if } r > 0.5, \end{cases}$$
$$\mathbf{A}(\mathbf{x},0) = \mathbf{I}, \qquad \mathbf{J}(\mathbf{x},0) = \mathbf{0}, \qquad r = \sqrt{x^2+y^2}.$$

The parameters of the GPR model are set to $c_s = c_h = 0$ and $\mu = \kappa = 0$. The computational domain $\Omega = [-1,1]^2$ is discretised with a primal mesh of 85344 triangles, and periodic boundary conditions are imposed everywhere. The numerical results obtained with the new hybrid FV/FE scheme using the local ADER-ENO approach are reported in Figure 14. The obtained solution shows a good agreement with the reference solution computed employing the 1D partial differential equation in radial direction with geometrical source terms equivalent to the compressible Euler system and solved using a second order TVD-FV scheme on a grid of 10^4 cells, [42].

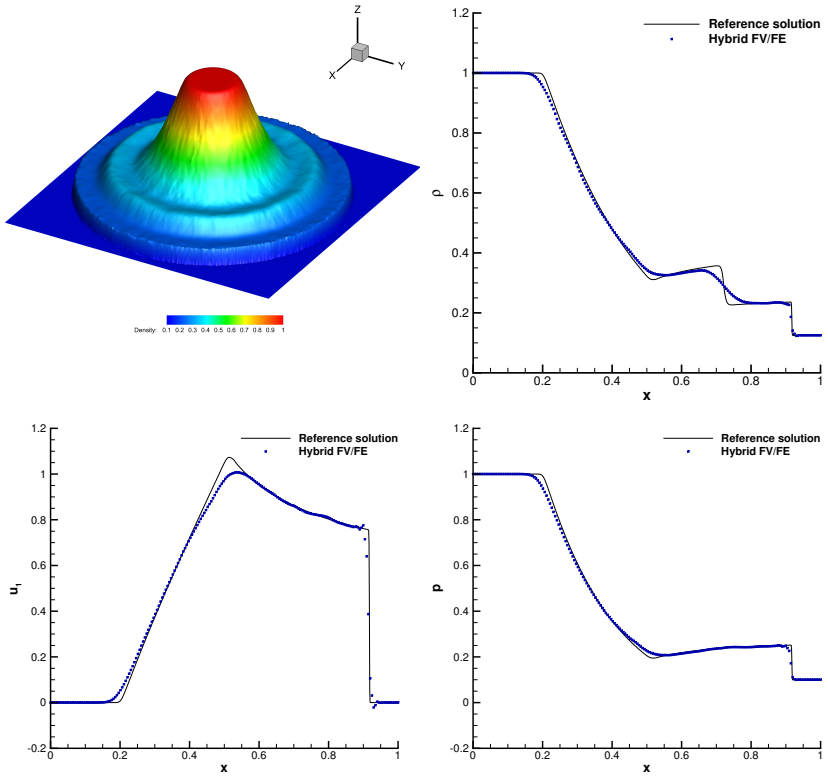

Fig. 14 Fluid circular explosion. Left top: elevated contour plot of the density field. From right top to right bottom: 1D cut in $x-$direction of the density, velocity component u_1 and pressure obtained using the hybrid FV/FE method for the weakly compressible GPR model with the local ADER-ENO approach and auxiliary artificial viscosity $c_\alpha = 0.5$ (blue squares). Reference solution (solid black line).

4.7.2 Solid circular explosion

To analyse the behaviour also in the solid limit, i.e., for $\tau_1 \to \infty$, $\tau_2 \to \infty$, we follow [14] and set $\tau_1 = \tau_2 = 10^{20}$, $\rho_0 = 1$, $c_v = 1.0$, $c_s = 1$, $c_h = 0.5$, $\gamma = 1.4$ and the initial condition

$$\rho(\mathbf{x},0) = 1, \quad u(\mathbf{x},0) = \mathbf{0}, \quad p(\mathbf{x},0) = \begin{cases} 2 \text{ if } r \leq 0.5, \\ 1 \text{ if } r > 0.5, \end{cases} \quad \mathbf{A}(\mathbf{x},0) = \mathbf{I}, \quad \mathbf{J}(\mathbf{x},0) = \mathbf{0}.$$

We run the simulation using the hybrid FV/FE scheme using the local ADER min-mod approach and an auxiliary artificial viscosity $c_\alpha = 0.5$. Again, periodic boundary conditions are set in all boundaries. The results obtained at time $t = 0.15$ with a fine grid of 1365504 primal triangular elements are reported in Figure 15. Moreover, Figure 16 reports the 1D cuts for the density, pressure, distortion component A_{11} and thermal impulse component J_1 along a 1D cut in $x-$direction. An excellent agreement is observed with the reference solution computed using a second order MUSCL-Hancock finite volume scheme, [81,14].

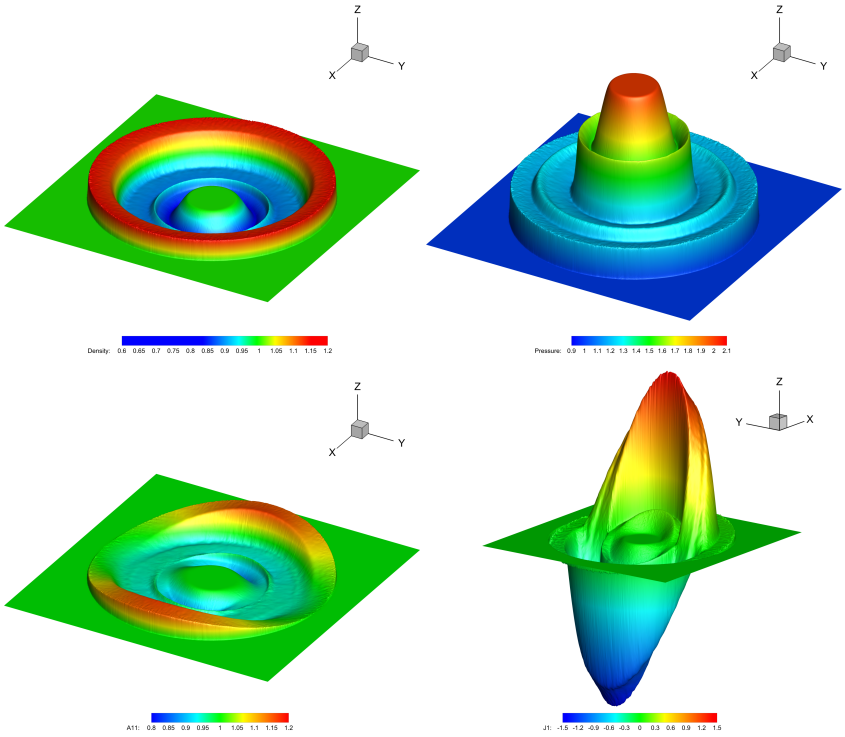

Fig. 15 Solid circular explosion. From left top to right bottom: elevated contour plots of the density, pressure, distortion component A_{11} and thermal impulse component J_1.

4.8 3D spherical explosion

To illustrate the extension of the proposed hybrid FV/FE methodology for the weakly compressible GPR model to the three-dimensional case, we study the 3D spherical explosion problem already employed in [4] to assess weakly compressible flows. The computational domain is a sphere of radius 1 centred in $(0,0,0)$ and discretised using a primal grid of 2280182 tetrahedra. As initial condition we set

$$\rho\left(\mathbf{x},0\right)=\begin{cases}2 & \text{if } r\leq 0.5,\\ 1.125 & \text{if } r>0.5,\end{cases}\qquad p\left(\mathbf{x},0\right)=\begin{cases}2 & \text{if } r\leq 0.5,\\ 1.1 & \text{if } r>0.5,\end{cases}$$
$$\mathbf{u}\left(\mathbf{x},0\right)=0,\qquad \mathbf{A}\left(\mathbf{x},0\right)=\mathbf{I},\qquad \mathbf{J}\left(\mathbf{x},0\right)=\mathbf{0},$$

with r the distance to the origin, and the model parameters are defined as $c_s = c_h = 0$ and $\mu = \kappa = 0$, which correspond to the fluid limit of the model. Dirichlet boundary conditions are imposed and the numerical simulation is carried out up to time $t = 0.25$. Figure 17 reports the results obtained using the LADER-ENO approach for the convective terms and auxiliary artificial viscosity $c_\alpha = 3$. We

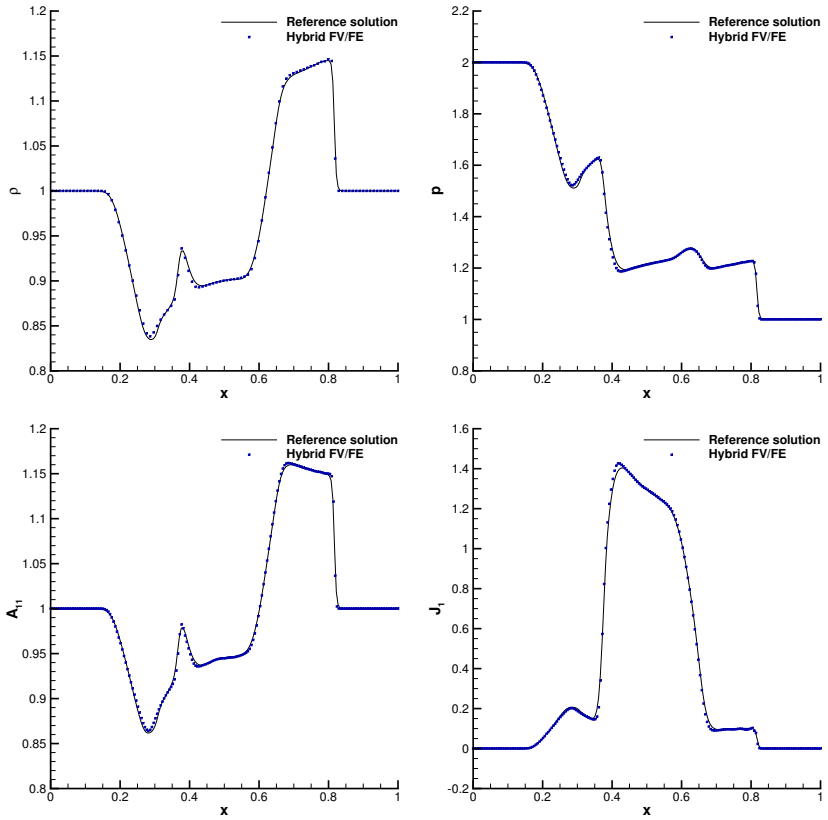

Fig. 16 Solid circular explosion. 1D cut in $x-$direction of the numerical solution obtained using the hybrid FV/FE method for the weakly compressible GPR model with the local ADER-MM approach and auxiliary artificial viscosity $c_\alpha = 0.5$ (blue squares). Reference solution obtained with a MUSCL-Hancock FV scheme [14] (solid black line). From left top to right bottom: density, pressure, distortion component A_{11} and thermal impulse component J_1.

observe a good agreement with the reference solution computed using a TVD-FV scheme for the 1D compressible Euler equations with appropriate geometrical source terms, [81].

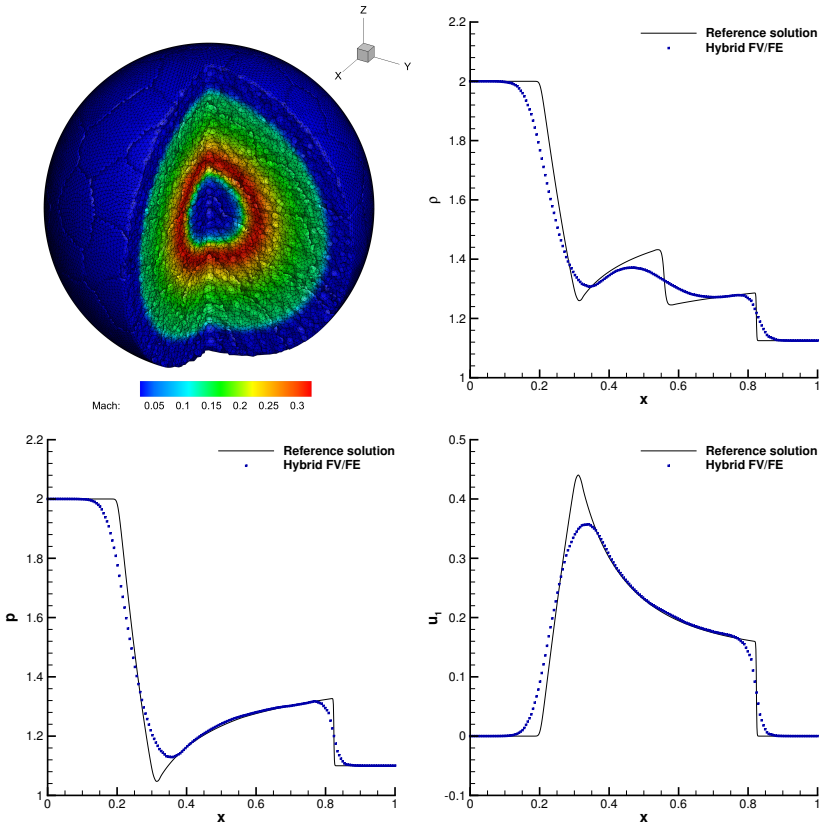

Fig. 17 3D spherical explosion. Left top: 3D mesh with MPI divisions and Mach number contours. From top right to bottom right: 1D cuts along the $x-$axis of the density, pressure, and velocity component u_1 obtained using the hybrid FV/FE method for the weakly compressible GPR model with the local ADER-ENO approach and auxiliary artificial viscosity $c_\alpha = 3$ (blue squares). Reference solution obtained with a FV-TVD scheme solving the 1D Euler equations (solid black line).

4.9 Smooth acoustic wave

One important difference between weakly compressible and incompressible flows is the presence of acoustic waves. To analyse the ability of the proposed semi-implicit FV/FE approach to capture acoustic waves properly we consider the smooth acoustic wave benchmark in [79, 4]. The initial condition is defined as

$$\rho\left(\mathbf{x},0\right)=1,\;\;\mathbf{u}\left(\mathbf{x},0\right)=0,\;\;p\left(\mathbf{x},0\right)=1+e^{-\alpha r^2},\;\;\mathbf{A}=\mathbf{I},\;\;\mathbf{J}=\mathbf{0},\;\;r=\sqrt{x^2+y^2}$$

and the model parameters are set to $\mu = \kappa = c_s = c_h = 0$. The computational domain $\Omega = [0, 2]^2$ is discretised employing a primal triangular grid formed by 131072 cells, and periodic boundary conditions are defined everywhere. The second order hybrid FV/FE scheme with ENO limiters is employed to get the solution at time $t = 1$. To generate a reference solution, we consider the 1D PDE in

radial direction with geometrical source terms equivalent to the compressible Euler system, which is solved using a second order TVD-FV scheme on a grid of 10^4 cells. Figure 18 shows an excellent agreement between both numerical results. Let us remark that even if this test case is characterised by a low Mach number, the compressibility still plays a primal role since we observe a steep acoustic wavefront propagating in radial direction. Moreover, using a semi-implicit approach leads to a CFL number depending only on the bulk flow velocity, so we circumvent the strong time step restriction of explicit Godunov-type solvers, which is related to the sound speed.

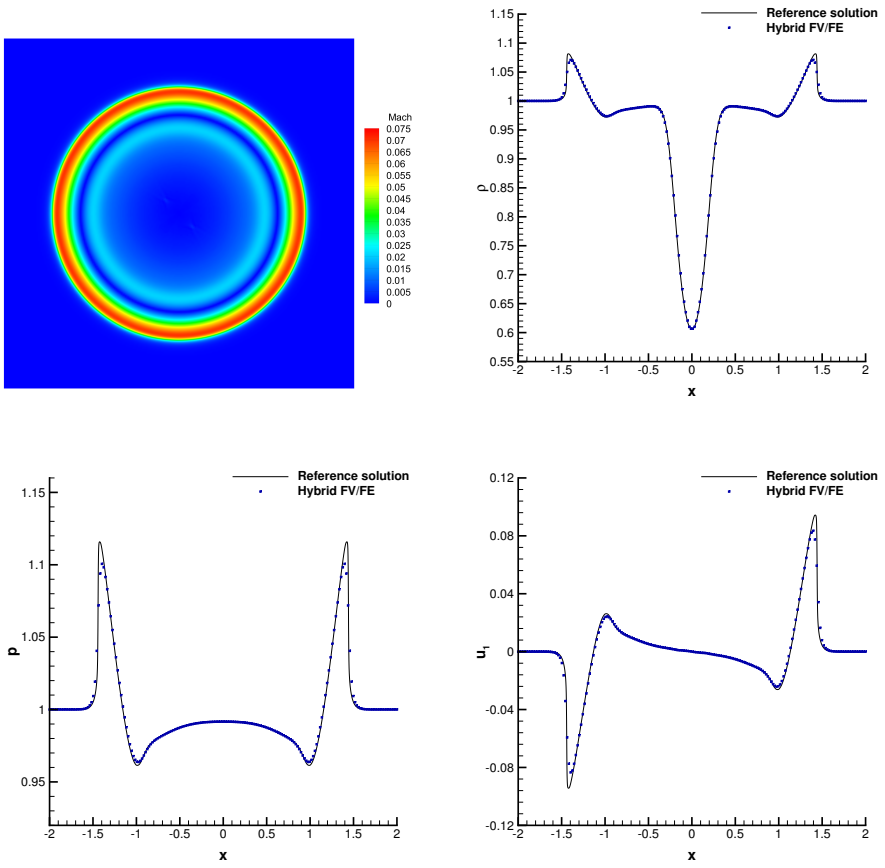

Fig. 18 Smooth acoustic wave. Left top: 2D Mach number contour plot obtained at time $t = 1$. From right top to right bottom: 1D cuts along $y = 0$ of the density, pressure and velocity component u_1 (blue squares). Reference solution computed with the TVD-FV scheme on a grid of 10^4 cells (black solid line).

5 Conclusions

We have presented a novel hybrid FV/FE methodology for solving the GPR model for continuum mechanics on unstructured meshes. From the compressible mathematical model and to simulate weakly compressible flows, we have derived two new formulations: the incompressible GPR model and a weakly compressible GPR model. Moreover, as for the original GPR model, able to address all Mach number flows appropriately by setting the model parameters, we can simulate both solids with large deformations and fluids. To discretise these systems, a splitting of the equations is performed, leading to a Poisson-type pressure system and a transport system containing convective terms and non-conservative products. This last system is solved using finite volume methods. Even if this part of the scheme is explicit, it is independent of the fast sound velocity waves, yielding a computationally efficient scheme in the low Mach regime. Moreover, to avoid the severe time-step restriction that may arise from the presence of stiff source terms in the distortion field and thermal impulse equations, an implicit finite volume method is employed for their discretisation. On the other hand, the pressure subsystem is solved using classical finite element methods, which are well known for their efficiency in solving Poisson-type problems. Finally, the intermediate momentum field computed within the transport stage of the algorithm is corrected to account for the new pressure, thus providing the momentum at the new time step. The final methodology has been successfully assessed employing a wide range of test cases, from solid mechanics benchmarks to the incompressible fluid limit of the equations, including the analysis of low Mach problems featuring small shocks.

In future, we plan to extend the former hybrid methodology to deal with fluid-structure iteration problems. To this end, following the methodology in [24] for the Navier-Stokes equations, the hybrid FV/FE method for the GPR model will also be developed in the ALE framework. Moreover, we plan to tackle the current second order in space - first order in time limitation devising a high order of accuracy hybrid method combining DG schemes and extended IMEX algorithms, [77, 11]. One important advantage of the proposed weakly compressible method, over all Mach number solvers, is its computational efficiency stemming from the use of a non-conservative pressure equation which produces a linear pressure system. However, this also yields a limitation: we are not able to deal with highly compressible flows. Therefore, in future, we will extend the hybrid methodology to solve a fully conservative formulation of the compressible GPR model, following similar approaches to those proposed for all Mach number flow solvers in the context of the Navier-Stokes equations, [27, 9]. Finally, we have analysed the AP property of the continuous model in the incompressible limit and shown that the proposed method attains second order of accuracy independently of the Mach number, but additional structural properties preserved by the continuous model are still neglected. Therefore, one future line of research is focused on the development of a hybrid methodology that exactly preserves the curl involution constraints of the distortion and thermal impulse fields, [43, 87], and we are interested on devising a hybrid approach also verifying thermodynamical compatibility at the discrete level, [2, 21].

Acknowledgements

SB acknowledges support from the Spanish Ministry of Science, Innovation and Universities (MCIN), the Spanish AEI (MCIN/AEI/10.13039/501100011033) and European Social Fund Plus under the project No. RYC2022-036355-I; from FEDER and the Spanish Ministry of Science, Innovation and Universities under project No. PID2021-122625OB-I00; and from the Xunta de Galicia (Spain) under project No. GI-1563 ED431C 2021/15. LR acknowledges the support from the Italian Ministry of Education, University and Research (MIUR) in the frame of the Departments of Excellence Initiative 2018–2027 attributed to DICAM of the University of Trento (grant L. 232/2016) and in the frame of the PRIN 2022 project *High order structure-preserving semi-implicit schemes for hyperbolic equations*. LR is member of the Gruppo Nazionale Calcolo Scientifico-Istituto Nazionale di Alta Matematica (GNCS-INdAM). The authors would like to acknowledge support from the CESGA, Spain, for the access to the FT3 supercomputer and to the CINECA award under the ISCRA initiative, for the availability of high performance computing resources and support (project IsB27_NeMesiS).

Views and opinions expressed are however those of the author(s) only and do not necessarily reflect those of the European Union. Neither the European Union nor the granting authorities can be held responsible for them.

Conflict of Interest

The authors declare that they have no conflict of interest.

Data availability

The data can be obtained from the authors on reasonable request.

References

1. E. Abbate, A. Iollo, and G. Puppo. An asymptotic-preserving all-speed scheme for fluid dynamics and nonlinear elasticity. *SIAM Journal on Scientific Computing*, 41:A2850–A2879, 2019.
2. R. Abgrall, S. Busto, and M. Dumbser. A simple and general framework for the construction of thermodynamically compatible schemes for computational fluid and solid mechanics. *Applied Mathematics and Computation*, 440:127629, 2023.
3. T. Barth and D. Jespersen. The design and application of upwind schemes on unstructured meshes. In *27th Aerospace sciences meeting*, 1989.
4. A. Bermúdez, S. Busto, M. Dumbser, J.L. Ferrín, L. Saavedra, and M.E. Vázquez-Cendón. A staggered semi-implicit hybrid FV/FE projection method for weakly compressible flows. *Journal of Computational Physics*, 421:109743, 2020.
5. A. Bermúdez, A. Dervieux, J. A. Desideri, and M. E. Vázquez-Cendón. Upwind schemes for the two-dimensional shallow water equations with variable depth using unstructured meshes. *Computer Methods in Applied Mechanics and Engineering*, 155(1):49–72, 1998.
6. A. Bermúdez, J. L. Ferrín, L. Saavedra, and M. E. Vázquez-Cendón. A projection hybrid finite volume/element method for low-Mach number flows. *Journal of Computational Physics*, 271:360–378, 2014.
7. S. Boscarino, G. Russo, and L. Scandurra. All Mach number second order semi-implicit scheme for the Euler equations of gasdynamics. *Journal on Scientific Computing*, 77:850–884, 2018.

8. W. Boscheri, S. Busto, and M. Dumbser. An all Mach number semi-implicit hybrid finite volume/virtual element method for compressible viscous flows on Voronoi meshes. 2024.
9. W. Boscheri, S. Busto, and M. Dumbser. An all mach number semi-implicit hybrid finite volume/virtual element method for compressible viscous flows on voronoi meshes. *Computer Methods in Applied Mechanics and Engineering*, 2024.
10. W. Boscheri, S. Chiocchetti, and I. Peshkov. A cell-centered implicit-explicit Lagrangian scheme for a unified model of nonlinear continuum mechanics on unstructured meshes. *Journal of Computational Physics*, 451:110852, 2022.
11. W. Boscheri, A. Chiozzi, M.G. Carlino, and G. Bertaglia. A new family of semi-implicit finite volume/virtual element methods for incompressible flows on unstructured meshes. *Computer Methods in Applied Mechanics and Engineering*, 414:116140, 2023.
12. W. Boscheri, G. Dimarco, R. Loubère, M. Tavelli, and M. H. Vignal. A second order all mach number IMEX finite volume solver for the three dimensional Euler equations. *Journal of Computational Physics*, 415:109486, 2020.
13. W. Boscheri and M. Dumbser. Arbitrary-Lagrangian-Eulerian one-step WENO finite volume schemes on unstructured triangular meshes. *Communications in Computational Physics*, 14:1174–1206, 2013.
14. W. Boscheri, M. Dumbser, M. Ioriatti, I. Peshkov, and E. Romenski. A structure-preserving staggered semi-implicit finite volume scheme for continuum mechanics. *Journal of Computational Physics*, 424:109866, 2021.
15. W. Boscheri, M. Dumbser, and R. Loubère. Cell centered direct Arbitrary-Lagrangian-Eulerian ADER-WENO finite volume schemes for nonlinear hyperelasticity. *Computers & Fluids*, 134–135(Supplement C):111–129, 2016.
16. W. Boscheri and L. Pareschi. High order pressure-based semi-implicit IMEX schemes for the 3D Navier-Stokes equations at all Mach numbers. *Journal of Computational Physics*, 434:110206, 2021.
17. W. Boscheri and M. Tavelli. High order semi-implicit schemes for viscous compressible flows in 3D. *Applied Mathematics and Computation*, 434:127457, 2022.
18. S. Busto, S. Chiocchetti, M. Dumbser, E. Gaburro, and I. Peshkov. High order ADER schemes for continuum mechanics. *Frontiers in Physics*, 8:32, 2020.
19. S. Busto and M. Dumbser. On thermodynamically compatible discontinuous Galerkin methods for continuum mechanics and turbulent shallow water flows. *Journal of Scientific Computing*, 93(2):56, 2022.
20. S. Busto and M. Dumbser. A staggered semi-implicit hybrid finite volume/finite element scheme for the shallow water equations at all Froude numbers. *Applied Numerical Mathematics*, 175:108–132, 2022.
21. S. Busto and M. Dumbser. A new class of simple, general and efficient finite volume schemes for overdetermined thermodynamically compatible hyperbolic systems. *Communications on Applied Mathematics and Computation*, pages 1–37, 2023.
22. S. Busto, M. Dumbser, I. Peshkov, and E. Romenski. On thermodynamically compatible finite volume schemes for continuum mechanics. *SIAM Journal on Scientific Computing*, 44:A1723–A1751, 2022.
23. S. Busto, M. Dumbser, and L. Río-Martín. Staggered semi-implicit hybrid finite volume/finite element schemes for turbulent and non-Newtonian flows. *Mathematics*, 9:2972, 2021.
24. S. Busto, M. Dumbser, and L. Río-Martín. An Arbitrary-Lagrangian-Eulerian hybrid finite volume/finite element method on moving unstructured meshes for the Navier-Stokes equations. *Applied Mathematics and Computation*, 437:127539, 2023.
25. S. Busto, J. L. Ferrín, E. F. Toro, and M. E. Vázquez-Cendón. A projection hybrid high order finite volume/finite element method for incompressible turbulent flows. *Journal of Computational Physics*, 353:169–192, 2018.
26. S. Busto, L. Río-Martín, M. E. Vázquez-Cendón, and M. Dumbser. A semi-implicit hybrid finite volume/finite element scheme for all Mach number flows on staggered unstructured meshes. *Applied Mathematics and Computation*, 402:126117, 2021.
27. S. Busto, L. Río-Martín, M.E. Vázquez-Cendón, and M. Dumbser. A semi-implicit hybrid finite volume/finite element scheme for all Mach number flows on staggered unstructured meshes. *Appl. Math. Comput.*, 402:126117, 2021.
28. S. Busto, M. Tavelli, W. Boscheri, and M. Dumbser. Efficient high order accurate staggered semi-implicit discontinuous Galerkin methods for natural convection problems. *Computers & Fluids*, 198:104399, 2020.

29. M.J. Castro, E.D. Fernández-Nieto, A.M. Ferreiro, and C. Parés. Two-dimensional sediment transport models in shallow water equations. A second order finite volume approach on unstructured meshes. *Computer Methods in Applied Mechanics and Engineering*, 198(33):2520 – 2538, 2009.
30. V. Casulli and D. Greenspan. Pressure method for the numerical solution of transient, compressible fluid flows. *Int. J. Numer. Methods Fluids*, 4:1001–1012, 1984.
31. S. Chiocchetti and M. Dumbser. An exactly curl-free staggered semi-implicit finite volume scheme for a first order hyperbolic model of viscous two-phase flows with surface tension. *Journal of Scientific Computing*, 94:24, 2022.
32. F. Cordier, P. Degond, and A. Kumbaro. An Asymptotic-Preserving all-speed scheme for the Euler and Navier-Stokes equations. *Journal of Computational Physics*, 231:5685–5704, 2012.
33. S. Dellacherie. Analysis of Godunov type schemes applied to the compressible Euler system at low Mach number. *Journal of Computional Physics*, 229:978–1016, 2010.
34. R.S. Dembo, S.C. Eisenstat, and T. Steihaug. Inexact Newton methods. *SIAM Journal on Numerical analysis*, 19(2):400–408, 1982.
35. F. Dhaouadi and M. Dumbser. A first order hyperbolic reformulation of the Navier-Stokes-Korteweg system based on the GPR model and an augmented Lagrangian approach. *Journal of Computational Physics*, 470:111544, 08 2022.
36. F. Dhaouadi and M. Dumbser. A structure-preserving finite volume scheme for a hyperbolic reformulation of the Navier–Stokes–Korteweg equations. *Mathematics*, 11(4), 2023.
37. M. Dumbser, D. S. Balsara, E. F. Toro, and C.-D. Munz. A unified framework for the construction of one-step finite volume and discontinuous Galerkin schemes on unstructured meshes. *Journal of Computational Physics*, 227(18):8209–8253, 2008.
38. M. Dumbser and V. Casulli. A conservative, weakly nonlinear semi-implicit finite volume scheme for the compressible Navier-Stokes equations with general equation of state. *Applied Mathematics and Computation*, 272:479–497, 2016.
39. M. Dumbser, I. Peshkov, E. Romenski, and O. Zanotti. High order ADER schemes for a unified first order hyperbolic formulation of continuum mechanics: Viscous heat-conducting fluids and elastic solids. *Journal of Computational Physics*, 314:824–862, 2016.
40. M. Dumbser, I. Peshkov, E. Romenski, and O. Zanotti. High order ADER schemes for a unified first order hyperbolic formulation of Newtonian continuum mechanics coupled with electro-dynamics. *Journal of Computational Physics*, 348:298–342, 2017.
41. M. Dumbser, I. Peshkov, and E. I. Romenski. *A Unified Hyperbolic Formulation for Viscous Fluids and Elastoplastic Solids*, pages 451–463. Springer International Publishing, 2018.
42. M. Dumbser and E.F. Toro. On universal Osher-type schemes for general nonlinear hyperbolic conservation laws. *Communications in Computational Physics*, 10(3):635–671, 2011.
43. F. Fambri, E. Zampa, S. Busto, L. Río-Martín, F. Hindenlang, E. Sonnendrücker, and M. Dumbser. A well-balanced and exactly divergence-free staggered semi-implicit hybrid finite volume/finite element scheme for the incompressible MHD equations. *Journal of Computational Physics*, 493:112493, 2023.
44. D. Ferrari, I. Peshkov, E. Romenski, and M. Dumbser. A unified SHTC multiphase model of continuum mechanics, 2024.
45. Message Passing Interface Forum, editor. *MPI: A Message-Passing Interface Standard.* 2021.
46. E. Gaburro, M. J. Castro, and M. Dumbser. Well-balanced Arbitrary-Lagrangian-Eulerian finite volume schemes on moving nonconforming meshes for the Euler equations of gas dynamics with gravity. *Mon. Not. R. Astron. Soc.*, 477(2):2251–2275, 2018.
47. U. Ghia, K.N. Ghia, and C.T. Shin. High-Re solutions for incompressible flow using the Navier-Stokes equations and a multigrid method. *Journal of Computational Physics*, 48(3):387–411, 1982.
48. S.K. Godunov. An interesting class of quasilinear systems. *Dokl. Akad. Nauk SSSR*, 139(3):521–523, 1961.
49. S.K. Godunov and E.I. Romenski. *Elements of Continuum Mechanics and Conservation Laws.* Kluwer Academic/ Plenum Publishers, 2003.
50. J. L. Guermond, P. Minev, and J. Shen. An overview of projection methods for incompressible flows. *Comput. Methods Appl. Mech. Eng.*, 195:6011–6045, 2006.
51. H. Guillard and A. Murrone. On the behavior of upwind schemes in the low Mach number limit: II. Godunov type schemes. *Computers & fluids*, 33(4):655–675, 2004.

52. H. Jackson. A fast numerical scheme for the Godunov-Peshkov-Romenski model of continuum mechanics. *Journal of Computational Physics*, 348:514–533, 2017.
53. H. Jackson and N. Nikiforakis. A numerical scheme for non-Newtonian fluids and plastic solids under the gpr model. *Journal of Computational Physics*, 387:410–429, 2019.
54. O. Kincl, I. Peshkov, M. Pavelka, and V. Klika. Unified description of fluids and solids in smoothed particle hydrodynamics. *Applied Mathematics and Computation*, 439:127579, 2023.
55. X. Li and C. Gu. An all-speed Roe-type scheme and its asymptotic analysis of low Mach number behaviour. *Journal of Computational Physics*, 227(10):5144–5159, 2008.
56. A. Lucca, S. Busto, and M. Dumbser. An implicit staggered hybrid finite volume/finite element solver for the incompressible Navier-Stokes equations. *East Asian Journal on Applied Mathematics*, 13:671–716, 2023.
57. A. N. Malyshev and E. I. Romenski. Hyperbolic equations for heat transfer. global solvability of the Cauchy problem. *Siberian Mathematical Journal*, 27:734–740, 1986.
58. C.D. Munz, M. Dumbser, and S. Roller. Linearized acoustic perturbation equations for low Mach number flow with variable density and temperature. *Journal of Computational Physics*, 224(1):352–364, 2007.
59. C. Parés. Numerical methods for nonconservative hyperbolic systems: a theoretical framework. *SIAM J. Numer. Anal.*, 44:300–321, 2006.
60. L. Pareschi and G. Russo. Implicit–Explicit Runge–Kutta schemes and applications to hyperbolic systems with relaxation. *Journal of Scientific computing*, 25:129–155, 2005.
61. J.H. Park and C.D. Munz. Multiple pressure variables methods for fluid flow at all Mach numbers. *International journal for numerical methods in fluids*, 49(8):905–931, 2005.
62. R. B. Pember, A. S. Almgren, J. B. Bell, P. Colella, M. Howell, and M. Lai. A high order projection method for the simulation of unsteady turbulent non premixed combustion in an industrial burner. In *Proceedings of the 8th International Symposium on Transport Phenomena in Combustion*, pages 16–20, 1995.
63. F. Pena and V. Sande. Feconv, 2022. https://victorsndvg.github.io/FEconv/description.xhtml (Last access: 10/2024).
64. I. Peshkov, W. Boscheri, R. Loubère, E. Romenski, and M. Dumbser. Theoretical and numerical comparison of hyperelastic and hypoelastic formulations for Eulerian non-linear elastoplasticity. *Journal of Computational Physics*, 387(C):481–521, 2019.
65. I. Peshkov, M. Dumbser, W. Boscheri, E. Romenski, S. Chiocchetti, and M. Ioriatti. Simulation of non-Newtonian viscoplastic flows with a unified first order hyperbolic model and a structure-preserving semi-implicit scheme. *Computers & Fluids*, 224:104963, 2021.
66. I. Peshkov and E. Romenski. A hyperbolic model for viscous Newtonian flows. *Continuum Mechanics and Thermodynamics*, 28:85–104, 2016.
67. L. Río-Martín, S. Busto, and M. Dumbser. A massively parallel hybrid finite volume/finite element scheme for computational fluid dynamics. *Mathematics*, 9:2316, 2021.
68. P. L. Roe. *Modelling of Discontinuous Flows*, volume 22. 1985.
69. E. Romenski, I. Peshkov, M. Dumbser, and F. Fambri. A new continuum model for general relativistic viscous heat-conducting media. *Philosophical Transactions of the Royal Society A: Mathematical, Physical and Engineering Sciences*, 378(2170):20190175, 2020.
70. E. Romenski, G. Reshetova, and I. Peshkov. Computational model for compressible two-phase flow in deformed porous medium. In Osvaldo Gervasi, Beniamino Murgante, Sanjay Misra, Chiara Garau, Ivan Blečić, David Taniar, Bernady O. Apduhan, Ana Maria A. C. Rocha, Eufemia Tarantino, and Carmelo Maria Torre, editors, *Computational Science and Its Applications – ICCSA 2021*, pages 224–236. Springer International Publishing, 2021.
71. E. Romenski, G. Reshetova, and I. Peshkov. Thermodynamically compatible hyperbolic model of a compressible multiphase flow in a deformable porous medium and its application to wavefields modeling. *AIP Conference Proceedings*, 2448(1):020019, 2021.
72. E. I. Romenski, D. Drikakis, and E. F. Toro. Conservative models and numerical methods for compressible two-phase flow. *Journal of Scientific Computing*, 42:68–95, 2010.
73. E. I. Romenski, A. D. Resnyansky, and E. F. Toro. Conservative hyperbolic formulation for compressible two-phase flow with different phase pressures and temperatures. *Quarterly of Applied Mathematics*, 65(2):259–279, 2007.
74. E.I. Romenski. Hyperbolic systems of thermodynamically compatible conservation laws in continuum mechanics. *Mathematical and computer modelling*, 28(10):115–130, 1998.
75. V. V. Rusanov. The calculation of the interaction of non-stationary shock waves and obstacles. *USSR Computational Mathematics and Mathematical Physics*, 1:304–320, 1962.

76. M. Tavelli and W. Boscheri. A new class of efficient high order semi-Lagrangian IMEX discontinuous Galerkin methods on staggered unstructured meshes. *Submitted*, 2024.
77. M. Tavelli, S. Chiocchetti, E. Romenski, A.A. Gabriel, and M. Dumbser. Space-time adaptive ADER discontinuous Galerkin schemes for nonlinear hyperelasticity with material failure. *Journal of computational physics*, 422:109758, 2020.
78. M. Tavelli and M. Dumbser. A staggered space-time discontinuous Galerkin method for the three-dimensional incompressible Navier-Stokes equations on unstructured tetrahedral meshes. *Journal of Computational Physics*, 319:294 – 323, 2016.
79. M. Tavelli and M. Dumbser. A pressure-based semi-implicit space-time discontinuous Galerkin method on staggered unstructured meshes for the solution of the compressible Navier-Stokes equations at all Mach numbers. *Journal of Computational Physics*, 341:341 – 376, 2017.
80. A. Thomann, G. Puppo, and C. Klingenberg. An all speed second order well-balanced IMEX relaxation scheme for the Euler equations with gravity. *Journal of Computational Physics*, 420:109723, 2020.
81. E. F. Toro. *Riemann solvers and numerical methods for fluid dynamics: A practical introduction*. Springer, 2009.
82. E. F. Toro, R. C. Millington, and L. A. M. Nejad. *Towards very high order Godunov schemes*, pages 907–940. Springer, 2001.
83. E. F. Toro and M. E. Vázquez-Cendón. Flux splitting schemes for the Euler equations. *Computers & Fluids*, 70:1–12, 2012.
84. A. Tyliszczak. High-order compact difference algorithm on half-staggered meshes for low Mach number flows. *Computers & Fluids*, 127:131 – 145, 2016.
85. D.R. van der Heul, C. Vuik, and P. Wesseling. A conservative pressure-correction method for flow at all speeds. *Computers & Fluids*, 32(8):1113–1132, 2003.
86. M. E. Vázquez-Cendón. Improved treatment of source terms in upwind schemes for the shallow water equations in channels with irregular geometry. *Journal of Computational Physics*, 148(2):497–526, 1999.
87. E. Zampa, S. Busto, and M. Dumbser. A divergence-free hybrid finite volume/finite element scheme for the incompressible MHD equations based on compatible finite element spaces with a posteriori limiting. *Applied Numerical Mathematics*, 198:346–374, 2024.

A Derivation of the weakly GPR model using the total energy equation

The GPR model for continuum mechanics is an overdetermined symmetric hyperbolic thermodynamically compatible system so that the total energy equation is obtained from equations (1a)-(1e) following the Godunov formalism, [48,49,66]. Consequently, the non-conservative pressure equation can also be obtained by employing the energy conservation law instead of the entropy equation, following a procedure similar to the one classically employed to get the weakly compressible flow model from the compressible Navier-Stokes equations. More precisely, to get (11e), we start multiplying the momentum equations by the corresponding dual variable u_i yielding

$$u_i \frac{\partial}{\partial t}\left(\rho u_i\right) + u_i \frac{\partial}{\partial x_k}\left(\rho u_i u_k\right) + u_i \frac{\partial}{\partial x_i} p + u_i \frac{\partial}{\partial x_k}\left(\sigma_{ik} + \omega_{ik}\right) = \rho g_i u_i,$$
$$\frac{\partial}{\partial t}\left(\frac{1}{2}\rho u_i^2\right) + \frac{\partial}{\partial x_k}\left(\frac{1}{2}\rho u_i^2 u_k\right) + u_i \frac{\partial}{\partial x_i} p + u_i \frac{\partial}{\partial x_k}\left(\sigma_{ik} + \omega_{ik}\right) = \rho g_i u_i.$$

Summing all momentum equations, we get

$$\frac{\partial}{\partial t}\left(\frac{1}{2}\rho\left|\mathbf{u}\right|^2\right) + \nabla\cdot\left(\frac{1}{2}\rho\left|\mathbf{u}\right|^2\mathbf{u}\right) + \mathbf{u}\cdot\nabla p + \mathbf{u}\cdot\nabla\cdot\left(\boldsymbol{\sigma}+\boldsymbol{\omega}\right) = \rho\mathbf{g}\cdot\mathbf{u}.$$

Subtracting this relation from the total energy equation and taking into account that

$$\nabla\cdot\left(\boldsymbol{\sigma}\mathbf{u}\right) = \mathbf{u}\cdot\nabla\cdot\boldsymbol{\sigma} + \boldsymbol{\sigma}\cdot\nabla\mathbf{u}, \quad \nabla\cdot\left(\boldsymbol{\omega}\mathbf{u}\right) = \mathbf{u}\cdot\nabla\cdot\boldsymbol{\omega} + \boldsymbol{\omega}\cdot\nabla\mathbf{u}, \quad \nabla\cdot\left(\mathbf{u}p\right) = p\,\nabla\cdot\mathbf{u} + \mathbf{u}\cdot\nabla p,$$

it results

$$\frac{\partial}{\partial t}\left(\rho E\right)-\frac{\partial}{\partial t}\left(\frac{1}{2}\rho\left|\mathbf{u}\right|^{2}\right)+\nabla\cdot\left(\rho E\mathbf{u}\right)-\nabla\cdot\left(\frac{1}{2}\rho\left|\mathbf{u}\right|^{2}\mathbf{u}\right)+p\,\nabla\cdot\mathbf{u}$$
$$+\boldsymbol{\sigma}\cdot\nabla\,\mathbf{u}+\boldsymbol{\omega}\cdot\nabla\,\mathbf{u}+\nabla\cdot\mathbf{q}=0.$$

Decomposing the total energy (5) into its four components and taking into account (6) and the equation of state for ideal gasses in E_4, (8), we get

$$\frac{\partial}{\partial t}\left(\frac{p}{\gamma-1}\right)+\nabla\cdot\left(\frac{p}{\gamma-1}\mathbf{u}\right)+\frac{\partial}{\partial t}\left(\rho E_2\right)+\nabla\cdot\left(\rho E_2\mathbf{u}\right)+\frac{\partial}{\partial t}\left(\rho E_3\right)+\nabla\cdot\left(\rho E_3\mathbf{u}\right)$$
$$+p\,\nabla\cdot\mathbf{u}+\boldsymbol{\sigma}\cdot\nabla\,\mathbf{u}+\boldsymbol{\omega}\cdot\nabla\,\mathbf{u}+\nabla\cdot\mathbf{q}=0.$$

Since $\gamma=\dfrac{c^2\rho}{p}$ and $\nabla\cdot\left(p\mathbf{u}\right)=p\,\nabla\cdot\mathbf{u}+\mathbf{u}\cdot\nabla\,p$, we obtain

$$\frac{\partial p}{\partial t}+\mathbf{u}\cdot\nabla\,p+\left(\gamma-1\right)\left(\frac{\partial}{\partial t}\left(\rho E_2\right)+\nabla\cdot\left(\rho E_2\mathbf{u}\right)+\frac{\partial}{\partial t}\left(\rho E_3\right)+\nabla\cdot\left(\rho E_3\mathbf{u}\right)\right)$$
$$+c^2\rho\,\nabla\cdot\mathbf{u}+\left(\gamma-1\right)\left(\boldsymbol{\sigma}\cdot\nabla\,\mathbf{u}+\boldsymbol{\omega}\cdot\nabla\,\mathbf{u}+\nabla\cdot\mathbf{q}\right)=0.$$

Hence, taking into account $\nabla\cdot\left(\rho\mathbf{u}\right)=\rho\,\nabla\cdot\mathbf{u}+\mathbf{u}\cdot\nabla\,\rho$, it yields

$$\frac{\partial p}{\partial t}+\mathbf{u}\cdot\nabla\,p+\left(\gamma-1\right)\left(\frac{\partial}{\partial t}\left(\rho E_2\right)+\nabla\cdot\left(\rho E_2\mathbf{u}\right)+\frac{\partial}{\partial t}\left(\rho E_3\right)+\nabla\cdot\left(\rho E_3\mathbf{u}\right)\right)$$
$$+c^2\,\nabla\cdot\left(\rho\mathbf{u}\right)-c^2\mathbf{u}\cdot\nabla\,\rho+\left(\gamma-1\right)\left(\boldsymbol{\sigma}\cdot\nabla\,\mathbf{u}+\boldsymbol{\omega}\cdot\nabla\,\mathbf{u}+\nabla\cdot\mathbf{q}\right)=0. \tag{46}$$

To get rid of the time derivative term on E_2, we first multiply (1c) by $\rho E_{A_{ik}}$, and sum over all equations of the distortion field components, obtaining

$$\rho E_{A_{ik}}\frac{\partial}{\partial t}A_{ik}+\rho E_{A_{ik}}\frac{\partial}{\partial x_k}\left(u_m A_{im}\right)+\rho E_{A_{ik}}u_j\frac{\partial}{\partial x_j}A_{ik}-\rho E_{A_{ik}}u_j\frac{\partial}{\partial x_k}A_{ij}$$
$$=-\frac{\rho}{\theta_1\left(\tau_1\right)}E_{A_{ik}}E_{A_{ik}},$$

hence

$$\rho\frac{\partial}{\partial t}E_2+\rho\mathbf{u}\cdot\nabla\,E_2+\rho E_{A_{ik}}\left(\frac{\partial}{\partial x_k}\left(u_m A_{im}\right)-u_m\frac{\partial}{\partial x_k}A_{im}\right)=-\frac{\rho}{\theta_1\left(\tau_1\right)}E_{A_{ik}}E_{A_{ik}}.$$

Adding (1a) multiplied by E_2,

$$E_2\frac{\partial}{\partial t}\rho+E_2\,\nabla\cdot\left(\rho\mathbf{u}\right)=0,$$

we get

$$\frac{\partial}{\partial t}\left(\rho E_2\right)+\nabla\cdot\left(\rho E_2\mathbf{u}\right)=-\rho E_{A_{ik}}A_{im}\frac{\partial}{\partial x_k}u_m-\frac{\rho}{\theta_1\left(\tau_1\right)}E_{A_{ik}}E_{A_{ik}}. \tag{47}$$

Substituting (47) in (46), we obtain

$$\frac{\partial p}{\partial t}+\mathbf{u}\cdot\nabla\,p+\left(\gamma-1\right)\left(-\rho E_{A_{ik}}A_{im}\frac{\partial}{\partial x_k}u_m-\frac{\rho}{\theta_1\left(\tau_1\right)}E_{A_{ik}}E_{A_{ik}}+\frac{\partial}{\partial t}\left(\rho E_3\right)\right.$$
$$\left.+\nabla\cdot\left(\rho E_3\mathbf{u}\right)\right)+c^2\,\nabla\cdot\left(\rho\mathbf{u}\right)-c^2\mathbf{u}\cdot\nabla\,\rho+\left(\gamma-1\right)\left(\boldsymbol{\sigma}\cdot\nabla\,\mathbf{u}+\boldsymbol{\omega}\cdot\nabla\,\mathbf{u}+\nabla\cdot\mathbf{q}\right)=0. \tag{48}$$

Following an analogous procedure, we next substitute the time derivative term in E_3. Multiplying (1d) by ρE_{J_k}, summing up all thermal impulse equations, and adding (1a) multiplied by E_3, lead to

$$\frac{\partial}{\partial t}\left(\rho E_3\right)+\nabla\cdot\left(\rho E_3\mathbf{u}\right)=-\rho E_{J_k}J_m\frac{\partial}{\partial x_k}u_m-\rho E_{J_k}\frac{\partial}{\partial x_k}T-\frac{\rho}{\theta_2\left(\tau_2\right)}E_{J_k}E_{J_k}. \tag{49}$$

Then substituting (49) in (48), we get

$$\begin{aligned}
&\frac{\partial p}{\partial t} + \mathbf{u}\cdot\nabla\, p + c^2\,\nabla\cdot(\rho\mathbf{u}) - c^2\mathbf{u}\cdot\nabla\,\rho + (\gamma-1)\,(\boldsymbol{\sigma}\cdot\nabla\,\mathbf{u} + \boldsymbol{\omega}\cdot\nabla\,\mathbf{u} + \nabla\cdot\mathbf{q}) \\
&\quad - (\gamma-1)\left(\rho E_{A_{ik}} A_{im}\frac{\partial}{\partial x_k}u_m + \rho E_{J_k} J_m \frac{\partial}{\partial x_k}u_m + \rho E_{J_k}\frac{\partial}{\partial x_k}T\right) \\
&\quad = (\gamma-1)\left(\frac{\rho}{\theta_1\,(\tau_1)}E_{A_{ik}}E_{A_{ik}} + \frac{\rho}{\theta_2\,(\tau_2)}E_{J_k}E_{J_k}\right).
\end{aligned}$$

Replacing $E_{J_k} = c_h^2 J_k$, $E_{A_{ik}} = c_s^2 A_{ij}\mathring{G}_{jk}$ in the left-hand side of the former equation leads to

$$\begin{aligned}
&\frac{\partial p}{\partial t} + \mathbf{u}\cdot\nabla\, p + c^2\,\nabla\cdot(\rho\mathbf{u}) - c^2\mathbf{u}\cdot\nabla\,\rho + (\gamma-1)\,(\boldsymbol{\sigma}\cdot\nabla\,\mathbf{u} + \boldsymbol{\omega}\cdot\nabla\,\mathbf{u} + \nabla\cdot\mathbf{q}) \\
&\quad - (\gamma-1)\left(\rho c_s^2 A_{ij}\mathring{G}_{jk} A_{im}\frac{\partial}{\partial x_k}u_m + \rho c_h^2 J_k J_m \frac{\partial}{\partial x_k}u_m + \rho c_h^2 J_k\frac{\partial}{\partial x_k}T\right) \\
&\quad = (\gamma-1)\left(\frac{\rho}{\theta_1\,(\tau_1)}E_{A_{ik}}E_{A_{ik}} + \frac{\rho}{\theta_2\,(\tau_2)}E_{J_k}E_{J_k}\right).
\end{aligned} \tag{50}$$

Finally, from (2) and (3), we observe that

$$\begin{aligned}
\boldsymbol{\sigma}\cdot\nabla\,\mathbf{u} = \sigma_{ik}\frac{\partial}{\partial x_k}u_i = A_{ji}\partial_{A_{jk}}(\rho E)\frac{\partial}{\partial x_k}u_i = \rho c_s^2 A_{mi}A_{mj}\mathring{G}_{jk}\frac{\partial}{\partial x_k}u_i, \\
\boldsymbol{\omega}\cdot\nabla\,\mathbf{u} = \omega_{ik}\frac{\partial}{\partial x_k}u_i = \rho c_h^2 J_i J_k\frac{\partial}{\partial x_k}u_i, \\
\nabla\cdot\mathbf{q} = \frac{\partial}{\partial x_k}\mathbf{q}_k = c_h^2\frac{\partial}{\partial x_k}(\rho J_k T) = c_h^2 T\frac{\partial}{\partial x_k}(\rho J_k) + c_h^2\rho J_k\frac{\partial}{\partial x_k}T.
\end{aligned}$$

Hence

$$\begin{aligned}
&\boldsymbol{\sigma}\cdot\nabla\,\mathbf{u} + \boldsymbol{\omega}\cdot\nabla\,\mathbf{u} + \nabla\cdot\mathbf{q} - \rho c_s^2 A_{ij}\mathring{G}_{jk}A_{im}\frac{\partial}{\partial x_k}u_m - \rho c_h^2 J_k J_m\frac{\partial}{\partial x_k}u_m \\
&\qquad -\rho c_h^2 J_k\frac{\partial}{\partial x_k}T = c_h^2 T\frac{\partial}{\partial x_k}(\rho J_k).
\end{aligned}$$

Substitution in (50) yields

$$\begin{aligned}
&\frac{\partial p}{\partial t} + u_k\frac{\partial}{\partial x_k}p + c^2\frac{\partial}{\partial x_k}(\rho u_k) - c^2 u_k\frac{\partial}{\partial x_k}\rho + c_h^2\,(\gamma-1)\,T\frac{\partial}{\partial x_k}(\rho J_k) \\
&\qquad = (\gamma-1)\left(\frac{\rho}{\theta_1\,(\tau_1)}E_{A_{ik}}E_{A_{ik}} + \frac{\rho}{\theta_2\,(\tau_2)}E_{J_k}E_{J_k}\right).
\end{aligned}$$

Hence, we have obtained the non-conservative pressure equation for the weakly compressible GPR model (11e).